

# Turbulent structure in free-surface jet flows

By D. T. WALKER<sup>1</sup>, C.-Y. CHEN<sup>1</sup> AND W. W. WILLMARTH<sup>2</sup>

<sup>1</sup>Department of Naval Architecture and Marine Engineering, University of Michigan,  
Ann Arbor, MI 48109-2145, USA

<sup>2</sup>Department of Aerospace Engineering, University of Michigan, Ann Arbor,  
MI 48109-2140, USA

(Received 1 March 1994 and in revised form 29 November 1994)

Results of an experimental study of the interaction of a turbulent jet with a free surface when the jet issues parallel to the free surface are presented. Three different jets, with different exit velocities and jet-exit diameters, all located two jet-exit diameters below the free surface were studied. At this depth the jet flow, in each case, is fully turbulent before significant interaction with the free surface occurs. The effects of the Froude number ( $Fr$ ) and the Reynolds number ( $Re$ ) were investigated by varying the jet-exit velocity and jet-exit diameter. Froude-number effects were identified by increasing the Froude number from  $Fr = 1$  to 8 at  $Re = 12\,700$ . Reynolds-number effects were identified by increasing the Reynolds number from  $Re = 12\,700$  to 102\,000 at  $Fr = 1$ . Qualitative features of the subsurface flow and free-surface disturbances were examined using flow visualization. Measurements of all six Reynolds stresses and the three mean velocity components were obtained in two planes 16 and 32 jet diameters downstream using a three-component laser velocimeter. For all the jets, the interaction of vorticity tangential to the surface with its 'image' above the surface contributes to an outward flow near the free surface. This interaction is also shown to be directly related to the observed decrease in the surface-normal velocity fluctuations and the corresponding increase in the tangential velocity fluctuations near the free surface. At high Froude number, the larger surface disturbances diminish the interaction of the tangential vorticity with its image, resulting in a smaller outward flow and less energy transfer from the surface-normal to tangential velocity fluctuations near the surface. Energy is transferred instead to free-surface disturbances (waves) with the result that the turbulence kinetic energy is 20% lower and the Reynolds stresses are reduced. At high Reynolds number, the rate of evolution of the interaction of the jet with the free surface was reduced as shown by comparison of the rate of change with distance downstream of the local Reynolds and Froude numbers. In addition, the decay of tangential vorticity near the surface is slower than for low Reynolds number so that vortex filaments have time to undergo multiple reconnections to the free surface before they eventually decay.

---

## 1. Introduction

Interest in the interaction of turbulent flow with a free surface has increased in recent years. A significant portion of this interest has come as a result of recent advances in remote sensing, which are expected to allow world-wide monitoring of maritime traffic in the foreseeable future. Techniques such as synthetic-aperture radar are capable of detecting the free-surface disturbances created by the flow about a surface ship many kilometres behind the ship, and sometimes hours after the ship has passed (see, e.g. Reed *et al.* 1990). At present, there is a significant lack of understanding of the nature

of the interaction of a turbulent shear flow, such as a ship wake, with a free surface. The purpose of the experimental investigation described in this paper is to increase our understanding of the interaction of turbulent shear flows with a free surface by study of a relatively simple flow in the laboratory. The ultimate goal is to use this knowledge to facilitate prediction of the free-surface features of a ship wake.

The specific flow selected for study of the interaction of a turbulent shear flow with a free surface is a submerged initially axisymmetric turbulent jet issuing beneath and parallel to a free surface. The parameters that define this free-surface flow are the Reynolds number  $Re = U_0 d/\nu$ , the Froude number  $Fr = U_0/(gd)^{1/2}$ , and the normalized depth of the jet beneath the free surface  $h/d$ . Here,  $U_0$  and  $d$  are the jet-exit velocity and diameter, respectively,  $h$  is the depth below the free surface,  $\nu$  is the kinematic viscosity,  $\rho$  is the fluid density and  $g$  is the gravitational acceleration. It should be noted that the definition of Froude number used here is different than that of Madnia & Bernal (1994), who used jet depth  $h$ , rather than  $d$ , as the characteristic length; this is discussed below in §3. A few investigations of this type of flow have been reported and they are described below. At present, no clear understanding exists regarding the effects of changes in the Reynolds and Froude numbers on the structure of turbulence and the nature of the surface deformations during interactions of a turbulent jet with a free surface.

Extensive turbulence measurements in axisymmetric turbulent jets in an infinite medium have been reported by Wygnanski & Fiedler (1969) and others. The study of turbulent jet flow near a free surface, however, has been relatively limited. Liepmann (1990) examined the interaction of a jet with a free surface (in which the laminar core of the jet was very near the free surface) and showed that the large-scale vortical structure of the jet was altered by the interaction. In the present study, as well as the other studies to be cited below, the jet was located further beneath the free surface and was fully turbulent when it first interacted with the free surface.

Swean *et al.* (1989) made measurements in a developing planar surface jet and noted a decrease in vertical velocity fluctuations near the free surface. A round turbulent jet issuing parallel to a free surface was examined by Madnia & Bernal (1994) using flow visualization and single-component hot-film measurements. Significant surface disturbances occurred where the large-scale structures in the jet first interact with the free surface. These disturbances form approximately plane waves which propagate away from the jet axis. The angle at which the waves propagate varied with jet exit velocity and jet depth – the angle increasing with increasing velocity or decreasing depth. They also noted the appearance of small circular dimples on the free surface using shadowgraph visualization. These dimples are typical of the signature of a vortex with its axis normal to the free surface (see Sterling *et al.* 1987) and indicate that vortex reconnection (where a vortex filament parallel to the surface breaks and ‘reconnects’ to its image vortex above the free surface) has occurred.

Anthony & Willmarth (1992) examined a circular jet, at a single Reynolds number and Froude number, issuing below and parallel to a free surface using a three-component laser velocimeter. They also noted that the vertical velocity fluctuations were damped near the free surface and identified several other interesting effects. Most notable was the existence of a flow outward, away from the jet axis in a thin layer near the free surface. This was identified in near-surface velocity measurements. It was concluded, on the basis of flow visualization, that this outward flow, or ‘surface current’, was comprised mainly of vortical structures ejected from the main jet. The origin of the surface current was not identified; however, a similar outflow will occur for a three-dimensional wall jet (Davis & Winarto 1980; Launder & Rodi 1983), where

the zero stress condition at the free surface has been replaced by the no-slip condition appropriate for a solid wall. (The no-slip condition does result in a boundary layer on the wall and a thicker surface-current layer.) Launder & Rodi (1983) attributed the spreading to the creation of mean streamwise vorticity due to either bending of vortex lines or inhomogeneities in the Reynolds stress field. As pointed out by Anthony & Willmarth (1992), the identification of the surface current in both the wall jets and free-surface jets indicates that the phenomenon is associated with the common condition of a vanishing surface-normal velocity at the surface, rather than the differing conditions on the tangential velocities at the surface.

An outward flow at the surface similar to that observed by Anthony & Willmarth (1992) was observed by Walker & Johnston (1991) in moderate- to high-Reynolds-number model-ship wakes using flow visualization, and by Hoekstra (1991) using velocity measurements. This suggests that the mechanisms of generation of this surface current layer are basic fluid dynamic phenomena associated with the interaction of a turbulent flow with the free surface. Evidence of vortex reconnection has also been observed in model-ship wakes by Walker & Johnston (1991).

Since the results of this study are intended to shed light on the behaviour of turbulent surface-ship wakes, it is important to understand what ranges of the Froude and Reynolds numbers are relevant in turbulent ship wakes. If it is assumed that the turbulent wake of a surface ship is made up primarily of the boundary layer from the ship, then twice the boundary-layer thickness at the stern is a reasonable approximate lengthscale for the large scales in the wake. Assuming that the ship is a flat plate 140 m in length moving at 30 knots (both length and velocity typical of a modern destroyer), the boundary-layer thickness at the trailing edge is about 1 m. The resulting Reynolds number for the wake is about  $3 \times 10^7$  and the Froude number is about  $3 \times 10^0$ . These values of Froude and Reynolds number hold at the origin of the wake. Further aft of the ship, the lengthscale for the wake increases and the velocity scale decreases. This results in a decrease in the local Froude number, eventually to zero, in the far wake. Classical scaling for an axisymmetric wake suggests that the Reynolds number will decrease also, but only slowly (see, e.g. Tennekes & Lumley 1972, p. 118).

Hence, a ship wake is a turbulent shear flow with Froude numbers ranging from zero up to order  $10^0$  and a Reynolds number on the order of  $10^7$ . In this study, the range of Froude numbers spans those which occur in ship wakes. For all of the previous jet studies, summarized above, the Reynolds numbers were of order  $10^4$ , or less. In this study, the Reynolds number range extends an order of magnitude beyond that previously examined. This is sufficient to identify any significant Reynolds-number effects in the interaction of turbulence with the free surface.

In this study we aim to characterize the turbulent structure in free-surface jet flows, identify the significant features of the interaction with the free surface and identify the effect of variations in the Reynolds and Froude numbers. To this end, three different jets, with different exit velocities and jet-exit diameters, all located two jet-exit diameters below the free surface are studied. At this depth the turbulent jet flow, in each case, is fully turbulent before significant interaction with the free surface occurs. Froude-number effects were identified by increasing the Froude number from  $Fr = 1$  to 8 at  $Re = 12700$ . Reynolds-number effects were identified by increasing the Reynolds number from  $Re = 12700$  to 102000 at  $Fr = 1$ . The three jet flows, then, include 'high-Reynolds-number' case ( $Re = 102000$ ,  $Fr = 1.0$ ), a 'high-Froude-number case' ( $Re = 12700$ ,  $Fr = 8.0$ ), and an 'intermediate' case ( $Re = 12700$ ,  $Fr = 1.0$ ). These names will be used to refer to the different cases. The exact conditions for the experiments are summarized in table 1.

Exit diameter $d$ (m)	Exit velocity $U_0$ (m s <sup>-1</sup> )	Depth to jet axis $h$ (m)	$Re = \frac{U_0 d}{\nu}$	$Fr = \frac{U_0}{(gd)^{1/2}}$	$h/d$
0.102	1.00	0.204	102000	1.0	2.0
0.0254	0.50	0.051	12700	1.0	2.0
0.00635	2.00	0.0127	12700	8.0	2.0

TABLE 1. Experimental conditions

## 2. Experimental apparatus and procedures

For part of this study, the jet apparatus used by Anthony & Willmarth (1992) was re-used, but the experiments were conducted in a different tank and with an additional larger nozzle. Results at high Reynolds number were obtained using a large-scale jet operating in the University of Michigan towing tank. For the high-Reynolds-number jet, the three-component laser velocimeter was the one used by Anthony & Willmarth; for the other two jets, a different three-component laser velocimeter was used. In what follows, the jets are briefly described, and a description of the different tanks in which they were operated is given. A shadowgraph technique and a laser-induced-fluorescence method, used to visualize the qualitative features of the flows, are then described. Another laser-based-fluorescence technique, used for visualization surface-elevation profiles, is then discussed. The laser velocimeter is then described followed by a discussion of the methods used for calculation of the turbulence statistics, then ensemble sizes and the averaging times.

### 2.1. Jet apparatus

Different combinations of Reynolds number and Froude number were obtained by using three different combinations of jet nozzle diameter and exit velocity (see table 1). (The 0.00635 m nozzle was used in the study of Anthony & Willmarth 1992 with the same exit velocity, 2 m s<sup>-1</sup>.) All of the jet nozzles were similar; the nozzle profile was a fifth-degree polynomial having specified diameter at inlet and exit and both zero slope and curvature at inlet and exit.

The 0.00635 m jet was supplied by a submersible pump feeding a constant-head tank. The 0.0254 m jet was supplied directly through the submersible pump owing to the limited height of the laboratory. Velocity measurements at the jet exit for this latter case showed that the flow was steady. In both cases, the flow rate was continuously monitored via a calibrated rotameter. This system is shown schematically in figure 1.

The 0.102 m jet (designed and built by W. W. W.) is driven by a four-bladed propeller located on the axis of the jet. Downstream of the propeller is an expansion, followed by a honeycomb flow straightener and several screens. The nozzle was constructed of fibreglass and has a contraction ratio of 9:1. This jet has a maximum exit velocity of 3 m s<sup>-1</sup> and is capable of attaining Reynolds numbers in excess of 300 000. Initial measurements showed a turbulence intensity of about 0.5% at the jet exit plane and no measurable swirl in the jet.

The design of all the jets was such that they were free to entrain fluid from all directions, in contrast to jets emanating from planar walls, e.g. the jet of Madnia & Bernal (1994).

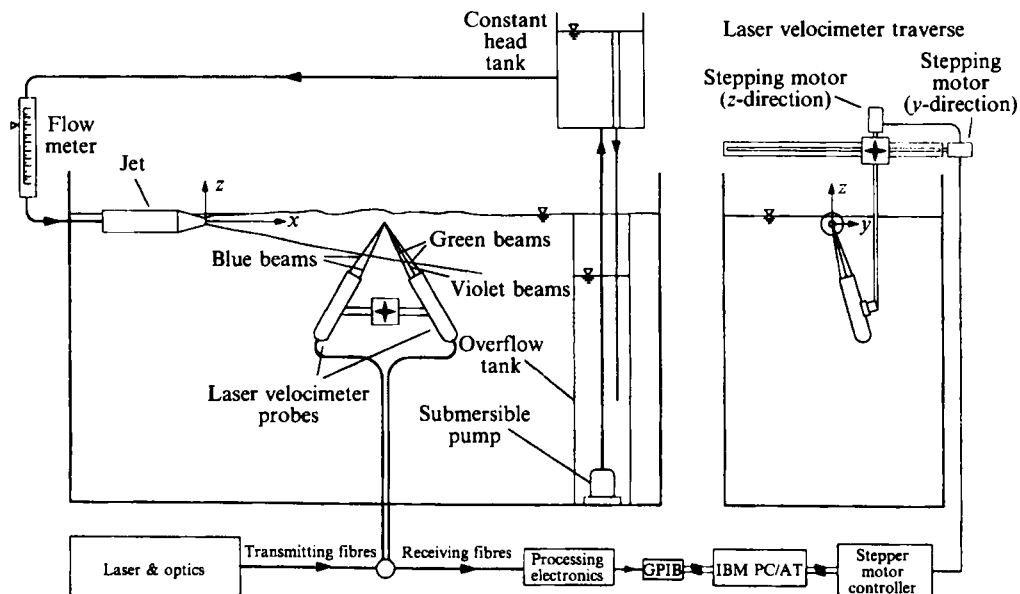


FIGURE 1. Schematic of experimental apparatus showing the jet and laser velocimeter system.

## 2.2. Tank facilities

The three jets were operated in two different tanks. Because of physical size of the 0.102 m jet, the measurements were made in the towing tank in the Marine Hydrodynamics Laboratory of the University of Michigan. The tank is 6.7 m wide, 3.1 m deep and 110 m long. To reduce seeding requirements for the laser velocimeter measurements, plastic curtains were located 48 jet diameters upstream and 128 diameters downstream of the jet exit plane. A swimming-pool-type skimmer, connected to a filter system, was operated at the downstream end of this region to continuously clean the free surface.

For the 0.0254 m and 0.00635 m jets, a smaller tank (3.05 m  $\times$  1.53 m  $\times$  1.22 m deep) was used. The pump for the jet was located in a smaller 'overflow' tank placed in the main tank (see figure 1). This overflow tank served to maintain a constant free-surface level during the experiments and also to continuously clean the free surface during the course of the experiment. For all cases, the tanks were at least  $60d$  wide,  $120d$  long and  $30d$  deep.

Surfactant contamination can qualitatively alter the interaction of turbulence with a free surface (see, e.g. Anthony & Willmarth 1992). The cleanliness of a free surface can be deduced by the presence, or absence, of the Reynolds ridge, which occurs at the boundary between the clean and contaminated regions of the surface (Hirsa & Willmarth 1994). A Reynolds ridge can be readily identified by visual inspection of the free surface. (The sharp change in surface slope associated with the ridge can be identified by looking at the reflection in the free surface of a regular geometric pattern.) The flow in the jet brings clean water to the surface above the turbulent core of the jet. Hence, if the surface is contaminated, a Reynolds ridge will exist on the free surface, somewhere between the turbulent core of the jet and the stationary fluid far away. For the experiments discussed here, the absence of a Reynolds ridge was verified visually and this was monitored during the course of the measurements. Therefore, the results presented below are free of surfactant effects. As an additional point of verification, all of the jets examined exhibited the same type of diverging flow near the free surface that

was seen in Anthony & Willmarth (1992). As was demonstrated in that study, the diverging flow near the surface would have been suppressed had the surface been contaminated.

### 2.3. Visualization techniques

Three visualization techniques were used for the examination of the qualitative features of the various jet flows. One, a shadowgraph technique, allows visualization of the free-surface features. Another, a laser-induced-fluorescence technique, is used for visualization of cross-sections of the turbulent jet. A third technique, also using laser-induced fluorescence, was used to examine the free-surface elevation profiles above the jet axis.

#### 2.3.1. Shadowgraph imaging

A shadowgraph technique was used to visualize the behaviour of the free surface for all the jet flow examined. This technique has been used in many investigations of free-surface flows; most recently for turbulent free-surface jets by Anthony & Willmarth (1992) and Madnia & Bernal (1994). In this implementation of the technique, a translucent screen was placed a small distance above the water surface and a point source of light was placed far below the surface. Any deformation of the free surface results in refraction of the light at the air-water interface and a corresponding change in the light intensity incident on the screen. Surface deformations which result in curvature act in a manner similar to a lens. For small curvatures, the effective focal length of the surface is  $f = R/(n-1)$ , where  $n$  is the index of refraction ( $n = 1.33$  for water) and  $R$  is the radius of curvature of the surface, positive for convex curvature (see, e.g. Hecht & Zajac 1974, p. 107). Local surface elevations, which generally will result in convex curvature, will cause bright regions on the shadowgraph screen, while surface depressions will result in dark regions. The distance of the screen above the free surface serves to select the range of surface curvatures to which the technique is sensitive. For a perfectly collimated light source, maximum intensity will occur for  $R = a(n-1)$ , where  $a$  is the distance of the screen above the water surface. For  $R > a(n-1)$ , as  $R$  increases, the intensity will decrease monotonically. For  $R < a(n-1)$  the intensity will decrease monotonically with decreasing  $R$ . Hence the brightest regions in a shadowgraph image correspond to surface disturbances with radii of curvature of about one-third the distance of the screen above the water surface.

The shadowgraph screen was 1.21 m square and was located 0.2 m above the free surface. The light source for these experiments was a 300 W tungsten flood lamp located 1.7 m below the free surface. Images of the shadowgraph screen were recorded at a framing rate of 30 Hz, but an electronic shutter was employed to yield an exposure time of 1 ms for each frame. Images from the shadowgraph experiments were recorded using a Panasonic TQ-3031F optical disk recorder. Individual frames were captured using an 8-bit Data Translation DT225-60 frame grabber operating in an Apple Macintosh IIx computer. Shadowgraph images were digitally enhanced by removing the background light intensity distribution which results from the point-source illumination.

#### 2.3.2. Subsurface fluorescent dye visualization

The subsurface evolution of the turbulent jets was visualized by marking the jet fluid with a fluorescent dye, fluorescein disodium salt. The evolution of the dye-marked fluid was examined using a two-dimensional sheet of laser light which was roughly 10 mm thick and oriented either normal to the jet axis or parallel to, and centred 5 mm below,

the free surface. The blue ( $0.4880\ \mu\text{m}$ ) line of an argon-ion laser was formed into a sheet using a cylindrical lens. As the fluorescent dye passed through the laser sheet, the emitted light yielded a cross-sectional view of the dye concentration distribution in the plane of the laser sheet. The dye concentration was limited to a few parts per million and therefore does not significantly change the density of the jet fluid.

The fluorescent emission from the dye was recorded digitally using a Cohu Inc. model 4115 ICCD camera connected to a Perceptics Inc. model PTG425 frame grabber. The frame grabber works in conjunction with a 32 MB buffer which allows capture of up to 128 frames ( $512 \times 512$  pixels) in real time. Some dye visualization images were digitally enhanced by adjusting the contrast to make the dye more visible.

### 2.3.3. Surface-elevation profiles

To examine the free-surface elevation profiles, a technique used to study two-dimensional breaking waves developed by Duncan (1983) was implemented. All the water in the tank was dyed using the same fluorescent dye used above. A laser sheet, formed using a cylindrical lens, was oriented perpendicular to the free surface and parallel to the jet centreline. This illuminated the water surface along the jet centreline from above. The laser sheet was about 1 mm thick at the free surface. For a sufficiently high dye concentration, all the laser energy is absorbed in a layer a few millimetres thick at the water surface. This energy is re-emitted as fluorescence and, if viewed from above the water surface, yields a high-contrast profile of the free surface. Again, the dye concentration used was low (several parts per million), and did not affect the fluid properties.

Both the high-Froude-number jet and the intermediate jet were examined using this approach. For the high-Froude-number jet, the high speeds encountered required a fast framing rate. For this flow a Kodak Ektapro imaging system was used which is capable of 1000 frames per second (f.p.s.) at a resolution of  $239 \times 192$  pixels. The camera was located 2 ft away from the laser sheet, and a 100 mm focal length  $f/2.8$  lens was used. This resulted in a field of view roughly 30 diameters wide. The vertical resolution of the image was 0.8 mm, which was acceptable for the large surface disturbances created by the high-Froude-number flow. The exposure time for each frame was 35  $\mu\text{s}$ . Several time series were acquired at the maximum framing rate (1000 f.p.s.).

## 2.4. Velocity measurements

### 2.4.1. Laser velocimeter

The velocity field of the jet was examined using two different three-component laser velocimeters. Both systems use three different lines of an argon-ion laser to obtain measurements of three independent components of velocity. The three colours used are green ( $0.5145\ \mu\text{m}$ ), blue ( $0.4880\ \mu\text{m}$ ), and violet ( $0.4765\ \mu\text{m}$ ); the green and blue beam pairs determined two velocity components in a plane, and the violet beam pair determined the third component which is perpendicular to this plane. Bragg cells were used to shift the frequency of one beam of each pair by 40 MHz in order to distinguish negative velocities on all components.

The laser velocimeter system used for the high-Reynolds-number jet was described in detail by Willmarth (1987) and Anthony & Willmarth (1992). For the two low-Reynolds-number jets, two 83 mm diameter TSI fibre-optically coupled LDV probes (a single-component probe and a two-component probe) were used (see figure 1). The angle between the two probes axes is nominally  $45^\circ$ , and the plane of the probes is  $15^\circ$  from vertical. Each beam pair formed an effective measuring volume approximately

65  $\mu\text{m}$  in diameter with a length-to-diameter ratio of approximately 14. The scattering particles used were titanium dioxide of rutile crystalline form and were approximately 3  $\mu\text{m}$  in size. The light scattered from the measuring volume was collected off-axis, each module receiving scattered light from transmitted beams of the other module. The coincident measurement volume is approximately a 3:1 ellipsoid with a diameter of 65–70  $\mu\text{m}$  and a length of roughly 200  $\mu\text{m}$ .

The signals from the photomultipliers were down-mixed to yield effective shift frequencies of 500 kHz on all three colours for the high-Froude-number jet. Effective shift frequencies of 200 kHz on green and blue, and 500 kHz on violet, were used for the intermediate case and the high-Reynolds-number case in order to maintain the resolution of the velocity measurements for the lower velocities encountered. The shift frequencies used were adequate to eliminate fringe bias (Whiffen, Lau & Smith 1979). This was verified for the intermediate and high-Froude-number cases by measuring velocities in the laminar flow at the jet exit with the jet rotated relative to the laser velocimeter system in a plane parallel to the free surface over the full range of angles present in the flow. The jet exit velocity was set to a level higher than any velocity attained in the turbulent flow field at the locations of interest, and for different angles the magnitude of the measured velocity and the validation rate remained constant. For the high-Reynolds-number case, fringe bias was not tested for directly, but the shift frequencies used were consistent with those which yielded good results for the other two cases.

The signals from the down-mixers were sent to counter-type signal processors (TSI 1980B). The outputs from the three counters were then checked for temporal coincidence. The length of the coincidence window was set equal to the average transit time of a particle passing through the measuring volume as recommended by Brown (1989). The valid data were transferred to a Lecroy MM8206A CAMAC digital memory and were then transferred over an IEEE-488 (GPIB) interface to an IBM PC-AT computer.

#### 2.4.2. Positioning

For the high-Reynolds-number jet, the laser velocimeter was traversed in a plane normal to the jet axis. The jet was moved along its axis to obtain measurements at different axial locations. For the other two cases, which used the laser velocimeter system described above, the jets were fixed and the laser velocimeter was traversed in three dimensions to obtain measurements. For all the cases, the measurement volume was traversed by means of rail-mounted slides and ballscrews driven by stepper motors. The motors were computer controlled and the measurement volume could be positioned with an accuracy better than 25  $\mu\text{m}$ .

Some of the results presented below were obtained at positions near the free surface. For flows where the surface is moving vertically, there is a possibility that the measurement volume will not be submerged continuously. If the measurement volume is completely above the water surface, then no measurements will be obtained. If the surface elevation and the velocity are correlated (as is the case with wave motion) then biased statistics may result.

For the intermediate case ( $Fr = 1.0$ ,  $Re = 12700$ ), the near-surface velocity measurements were done at a distance of 1.12 mm below the free surface. The root-mean-square surface elevation was estimated to be 0.2 mm, based on the results from the surface-elevation visualization technique described above in §2.3.3 (implemented with four times the resolution). For this case, it is clear that the measurement volume will always be fully immersed.

For the high-Froude-number case, large surface disturbances are present. Table 2 summarizes relevant information regarding the location of the measurement volume relative to the free surface, as well as the mean and r.m.s. surface elevations for this case at  $x/d = 16$  and  $32$ . These  $x/d$ -locations correspond to the downstream locations where velocity measurements were made. The measurement-volume locations refer to the centre of the volume. The last two columns show the probability that the measurement volume is at least partially immersed, and the probability that it is fully immersed at any given time for the two locations. These estimates are based on Gaussian statistics. From these data, it is clear that at  $x/d = 16$  the measurement volume will be at least partially immersed, and therefore capable of producing measurements, more than 90% of the time. For  $x/d = 32$ , the r.m.s. surface elevation is smaller than the measurement resolution. The smallest measurable r.m.s. surface elevation for this system is approximately 0.4 mm (or  $0.0630d$ ), and so this value is included in table 2 for  $x/d = 32$ . Using this value, the measurement volume is estimated to be at least partially immersed 78% of the time. This could lead to bias errors in the statistics.

The free surface will potentially drop below the position of the measurement volume as a wave trough passes the measurement location. As a result, the velocities which occur beneath the wave trough will not be measured. At this position, the free surface is at its lowest extreme, and the vertical velocity ( $W$ ) is near zero. Therefore, if this mechanism is causing a bias in the velocity data, there should be data missing from histograms of the measured  $W$  near  $W = 0$ . As an additional check, then, the histograms for  $W$  were examined for all the near-surface measurements. There are no apparent 'missing' data near  $W = 0$  in the histograms, and there is no discernable difference near  $W = 0$  in the histograms for data near the free surface compared to those further from the surface.

Since the measurement volume spends a substantial fraction of the time immersed, and there is no evidence of bias in the  $W$  histograms, we conclude that bias errors of this type in the data presented below are minimal, at most.

#### 2.4.3. Data acquisition and analysis

The data reported below are based on ensembles of individual realizations of the instantaneous, three-component velocity vector. Initially, the mean and standard deviation for each measured velocity component were calculated. Realizations that were more than three standard deviations removed from the mean on any component were eliminated. This usually resulted in the elimination of at most about 0.5% of the data points from the data set. The velocities were then resolved into the appropriate coordinate system and final statistics were calculated. All final statistics were corrected for velocity bias by weighting each velocity measurement with the reciprocal of the magnitude of the instantaneous velocity vector as proposed by McLaughlin & Tiederman (1973). This bias correction is appropriate when the projected area of the measurement volume does not vary over the range of flow angles encountered.

The results for the high-Froude-number jet were calculated using ensembles of 2000 elements. This generally resulted in an averaging time of about ten minutes, and little scatter was seen in the resulting turbulence statistics.

For a turbulent jet, the lengthscale for the large-scale structures at a given streamwise location (measured in terms of jet diameters) is some multiple of the jet diameter. For the three different jets examined here, then, the size of the large structures for the high-Reynolds-number case is four times that for the intermediate case which, in turn, is four times that for the high-Froude-number case. For a given

$x/d$	Mean surface elevation $\bar{z}_s/d$	R.m.s. surface elevation $z'_s/d$	Uppermost measurement location $z_m/d$	$\frac{\bar{z}_n - z_m}{d}$	Probabilities	
					Fully immersed	Partially immersed
16	2.021	0.0667	1.960	0.0606	0.82	0.92
32	1.922	0.0630†	1.960	0.0321	0.70	0.78

† This value corresponds to the minimum measurable r.m.s. surface elevation.

TABLE 2. Data for surface velocity measurements in the high-Froude-number jet

seed particle density, then, there are fewer particles per large structure in the high-Froude-number jet than in the intermediate case which, in turn has fewer particles per large structure than in the high-Reynolds-number case. As a result, for a given ensemble size (say 2000 elements) there are more large-scale structures represented in the high-Froude-number jet than in the other two cases. Averaging over more large structures results in more reliable statistics and less scatter in the data. To acquire data for an equivalent number structures in the intermediate case, at the same seeding density, ensembles must be four times as large (8000 elements). For the high-Reynolds-number jet ensembles must be four times larger still (32000 elements). While the ensemble sizes quoted here are not unreasonable, the fact that velocities vary from one case to the next causes a problem. The high-Froude-number jet has the largest velocities and, hence, the largest measurement rate of the three jets at any location. The measurement rate for the high-Reynolds-number case is lower by a factor of two and the intermediate case has the lowest (by another factor of two). The increase in ensemble size required to obtain a given number of large-scale structures, coupled with the reduction in measurement rate, causes the ten minutes required to acquire data at each point in the high-Froude-number jet to increase to nearly three hours in the intermediate case and six hours in the high-Reynolds-number jet.

At this rate, for the intermediate case, a single profile of thirty spatial locations would require more than three days of continuous running, which is unacceptably long in terms of maintaining optimum experimental conditions (particularly keeping the free surface free of contaminants). To ensure that the measurements sampled a sufficient number of large-scale structures at each location, but that a profile could be completed in a reasonable time, the laser velocimeter was sequentially scanned through a series of measurement locations, collecting fifty realizations at each location. Statistics were calculated based on 2000 point ensembles and the scans were repeated until the entire ensemble was acquired. This ensured that at least forty or so separate large-scale structures were sampled and resulted in reasonably well-converged statistics.

The measurements in the high-Reynolds-number jet were done first, before the above-discussed effects were fully appreciated. For this case, the large volume of water seeded resulted in significantly lower seed densities than in the other cases and substantially lower data rates. The ensemble size used for the calculation of statistics was 500. The number of large-scale structures represented in the statistics is probably not quite large enough, and it is clear in the results presented below that the statistics for this case are not quite as well-converged as the other two cases. This increased scatter, however, does not alter the major results of the study.

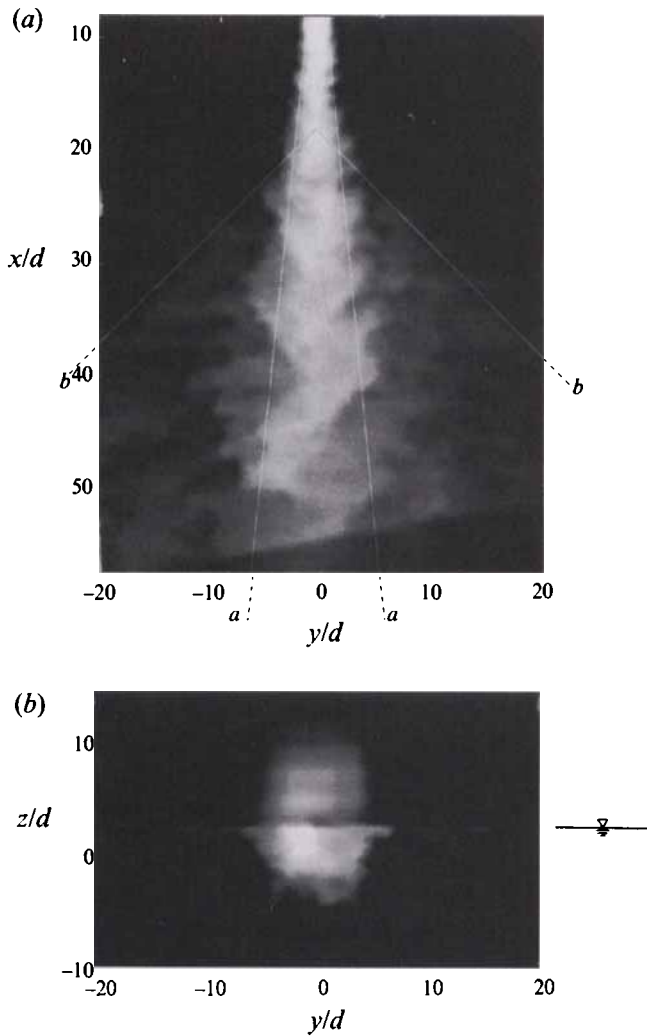


FIGURE 2. Fluorescent dye visualization showing development of the jet: (a) plan view; (b) end view, looking upstream at  $x/d = 32$ . Lines a-a correspond to  $y/x = 0.10$  and show the extent of the turbulent 'core' of the subsurface jet. Lines b-b indicate the extent of the diverging flow at the surface. The lateral extent of the field of view is 40 jet-exit diameters for both images. For (a), the laser sheet is 10 mm thick and centred 5 mm below the free surface and the top edge of the image corresponds to  $x/d = 8$ .

### 3. Results

For this study, water was the working fluid and the air-water interface will be referred to as the free surface. In the velocity measurements presented below, instantaneous velocities are designated using upper-case letters ( $U$ ,  $V$ ), fluctuations about the mean use lower-case letters ( $u$ ,  $v$ ), mean quantities are indicated by an overbar ( $\bar{U}$ ,  $\bar{V}$ ,  $\overline{uv}$ ), and root-mean-square (r.m.s.) velocities are designated using a prime ( $u'$ ,  $v'$ ). In these results,  $x$  is distance measured along the jet axis with  $x = 0$  at the jet exit plane; the positive  $x$ -direction will be referred to as the streamwise direction (see figure 1) and the corresponding velocity component  $U$  is the streamwise velocity. The surface-normal direction is defined as the  $z$ -direction, positive upward, with the origin on the jet axis. This will be referred to as the vertical direction with velocity

component  $W$ . The transverse, or horizontal, coordinate is  $y$ . The origin is again at the jet axis and the positive direction is defined so as to result in a right-handed coordinate system. The transverse velocity is given the symbol  $V$ . For all cases the jet issued parallel to the free surface and the jet axis was located a distance  $h = 2d$  below the free surface. This places the free surface at  $z = 2d$ .

Classical scaling arguments for a round turbulent jet in an infinite medium (a deep jet) show that the maximum velocity in a turbulent jet is proportional to  $x^{-1}$  while the characteristic length (usually the half-width at half the maximum velocity) is proportional to  $x$  (see, e.g. Tennekes & Lumley 1972, p. 130). For a self-preserving turbulent jet, therefore, universal behaviour will be found in the profiles of turbulence quantities if vertical and lateral distances ( $z$  and  $y$ ) are normalized by  $x$ , and velocities are normalized by  $U_0 d/x$ . Presentation of the data in this manner will allow ready comparison of the evolution of the near-surface jet to the self-preserving behaviour of a deep jet. It is also a consistent normalization for comparing the different cases to be examined in this study, and for examining the streamwise evolution of the jet for a given set of conditions. (Madnia & Bernal 1994 proposed scaling for free-surface jets using the jet depth  $h$ . This scaling applies only for  $x/h > 32$  and so is inappropriate for the results of this study which were obtained for  $x/h \leq 16$ , i.e.  $x/d \leq 32$ .)

The classical scaling also provides an interpretation for the different definitions of the Froude number used in Madnia & Bernal (1994) and presented above in §1. To examine the behaviour of the jet locally, the appropriate Froude number is one based on the local characteristic velocity and lengthscale of the jet at the location in question. For a deep jet (which is representative of the behaviour of the jet until it interacts with the free surface), the local characteristic velocity is given by  $U_c = AU_0 d/x$  and the local characteristic length is given by  $l_c = Bx$ , where  $A$  and  $B$  are non-dimensional constants. The local Froude number is then

$$Fr_{local} = \frac{U_c}{(2gl_c)^{1/2}} = \left( \frac{A}{(2B)^{1/2}} \right) \left( \frac{U_0}{(gx)^{1/2}} \right) \left( \frac{d}{x} \right).$$

Far downstream of the initial interaction of the jet with the free surface, the local Froude number approaches zero and no surface waves are generated. Before the interaction, there are no surface waves generated, and so the local Froude number is irrelevant. If we are interested in the surface disturbances generated by the initial interaction of the large structures of the jet with the free surface, then they will be characterized by the local Froude number at the location of the initial interaction. The initial interaction of the large-scale structures with the free surface occurs roughly when  $l_c = h$ . This occurs at  $x = h/B$ , and the local Froude number at the initial interaction location is

$$Fr_{local} = \frac{AB}{\sqrt{2}} \left( \frac{U_0}{(gh)^{1/2}} \right) \left( \frac{d}{h} \right) = \frac{AB}{\sqrt{2}} \left( \frac{U_0}{(gd)^{1/2}} \right) \left( \frac{d}{h} \right)^{3/2}.$$

Here, the middle term is written in terms of the depth Froude number used by Madnia & Bernal (1994) and the term on the right-hand side uses the Froude number based on jet-exit conditions defined in §1. In either case, the initial interaction of the jet with the free surface is characterized by the given Froude number and the depth of the jet.

In what follows, we will first examine qualitative behaviour using shadowgraph images of the free-surface disturbances and laser-induced-fluorescence images of the jet cross-section. Visualization of free-surface elevation profiles above the jet axis will then be presented. Profiles of turbulence quantities were obtained at two downstream

locations,  $x/d = 16$  and  $32$ . The closer location,  $x/d = 16$ , is just downstream of where the jet begins to interact with the free surface;  $x/d = 32$  is far enough downstream that the surface current identified by Anthony & Willmarth (1992) is well established. Vertical profiles were obtained in the symmetry plane of the jet ( $y = 0$ ) and horizontal profiles were obtained at  $z/d = 1.96$ , just below the undisturbed free surface ( $z/d = 2$ ). Mean velocities are presented first, followed by quantities related to the Reynolds stresses.

One of the three cases examined, the high-Froude-number jet, was at nominally the same conditions as were examined by Anthony & Willmarth (1992). These experiments were repeated for two reasons. First, the data of Anthony & Willmarth contain no near-surface measurements at  $x/d = 16$ . This required additional data to be acquired in the present study to enable a complete comparison. Second, the Anthony & Willmarth experiments were conducted with a jet depth of  $h/d \approx 2$ . The exact depth was  $h/d = 2.1$  (D. G. Anthony, private communication) and the near-surface measurements were made at  $z/d = 2.0$ . The results of this study reported below were obtained for  $h/d = 2.0$  and near-surface measurements were obtained at  $z/d = 1.96$ , with both positions accurate to 1% or better. Vertical profiles in the symmetry plane of the jet ( $y = 0$ ) in the present study for this equivalent case agree well with those of Anthony & Willmarth, except very near the free surface. The horizontal profiles just below the undisturbed free surface do not agree as well. In particular, the  $\bar{V}$  data of Anthony & Willmarth are as much as a factor of two lower near the surface. In the thin surface-current layer, the velocity gradient are quite large, as shown by Anthony & Willmarth. The difference in the depth of the measurement locations below the free surface, along with the larger jet depth, may account for a large proportion of the observed difference in near-surface behaviour.

### 3.1. Qualitative visualization

To establish a framework for interpretation of the quantitative measurements of turbulent structure (which will be presented below), visualization of the qualitative features of the various jet flows was done. Shadowgraph imaging of the free surface was used to identify differences in the free-surface features of the jets. Dyeing the jet fluid allowed visualization of the downstream evolution of the jet and the diverging flow at the surface.

Figure 2 shows fluorescent-dye visualization of the high-Froude-number jet. The plan view (figure 2*a*) shows the extent of the diverging flow at the surface. The horizontal extent of the image shown is 40 jet-exit diameters and the top edge of figure 2(*a*) corresponds to  $x/d = 8$ . The diverging flow starts a small distance downstream of the location of the initial interaction of the jet with the free surface and is indicated by the lines shown in the figure. Also shown on figure 2(*a*) are dashed lines corresponding to  $y/x = 0.10$ , roughly indicating the extent of the turbulent 'core' of the jet beneath the free surface. Figure 2(*b*) shows an end view of the jet, looking upstream. (The free surface is at  $z/d = 2$ ; the image above this location is a reflection of the subsurface flow.) The section shown corresponds to  $x/d = 32$  and clearly shows the diverging flow at the surface, as well as the turbulent core of the jet beneath the free surface. The intermediate case yielded very similar results and is not presented here. The high-Reynolds-number case was of such large scale that similar visualization was impractical.

Observation of time sequences of the subsurface view shown in figure 2(*b*) shows that the instantaneous outward flow of dyed fluid at the free surface on the right-hand side of the jet often correlates with clockwise rotation in the fluid just below the free

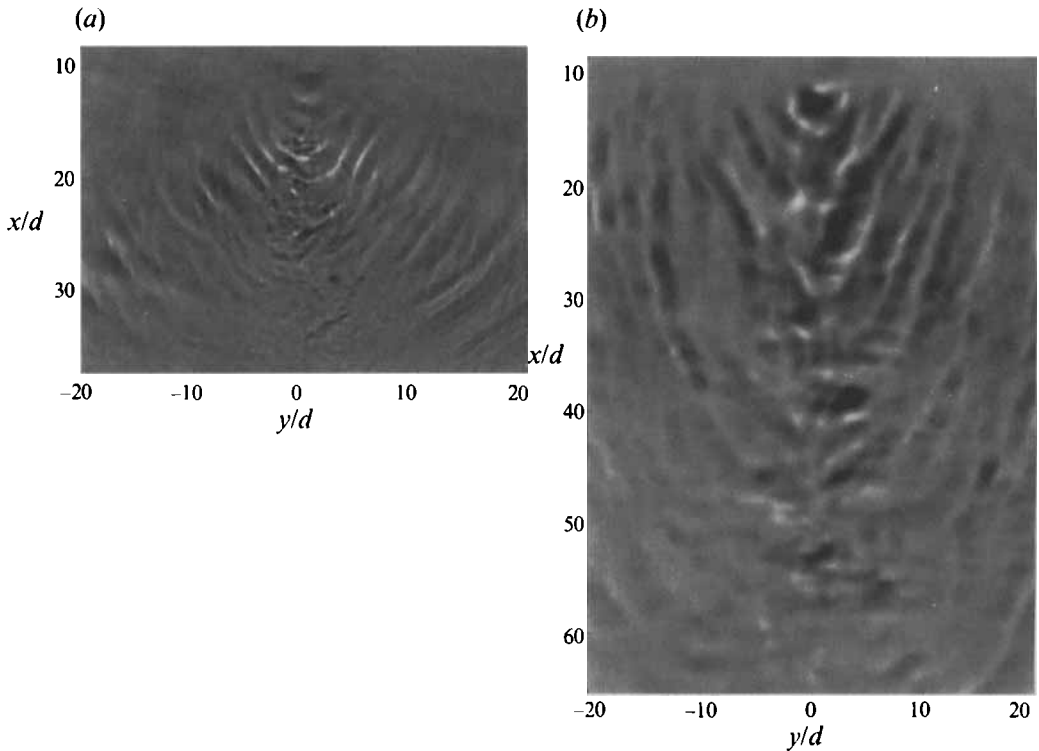


FIGURE 3. Shadowgraph visualization of the free-surface disturbances generated by the jet: (a)  $Re = 12700$ ,  $Fr = 1.0$ ; (b)  $Re = 12700$ ,  $Fr = 8.0$ . The lateral extent of the field of view is 40 jet-exit diameters for both cases. The top edge of each image corresponds to  $x/d = 8$ .

surface (seen in the dye pattern). Outward flow to the left of the jet correlates with counterclockwise rotation. (This is even more evident at  $x/d = 64$ , due to the larger lengthscales and longer timescales present.) This indicates that the diverging flow on the surface results, at least in part, from the interaction with the free surface of streamwise vorticity (or vorticity with a streamwise component). This interaction could be described as mutual induction between the vorticity in the subsurface flow, and its correlated 'image' above the free surface.

Shadowgraph visualization of the free-surface disturbances is shown in figures 3 and 4. Figure 3 shows the results for the intermediate case (figure 3a) and the high-Froude-number case (figure 3b). In this figure, the width of each field of view is also 40 jet-exit diameters and the top edge of the image again corresponds to  $x/d = 8$ . For the intermediate case, the initial interaction of the jet with the free surface occurs at about  $x/d = 10$ – $12$ . Waves generated by this initial interaction propagate radially outward initially, but as they propagate into the low-velocity fluid surrounding the jet, they are refracted by the velocity gradient (in a manner similar to that described by Longuet-Higgins & Stewart 1961 for a plane wave interacting with a step change in velocity). This refraction turns the waves until they are propagating obliquely away from the jet axis.

Downstream of the initial interaction (in the lower half of the image), surface deformations resulting from the subsurface turbulent flow are evident, but there is no significant wave generation. The same classical scaling arguments cited above can be used to understand the degree to which the turbulent jet flow can generate waves at

various downstream distances. The linear increase in the jet width and inverse dependence of the maximum velocity on streamwise distance from the jet origin yield a constant Reynolds number for the jet. These same dependencies results in a local Froude number, based on jet width and maximum velocity, which is proportional to  $x^{-3/2}$ . As a result, the turbulent flow's ability to generate waves decreases with increasing streamwise distance.

The high-Froude-number case, shown in figure 3(b), stands in stark contrast to the low-Froude-number flow shown in figure 3(a). There are waves being generated further downstream, as expected due to the higher initial Froude number. There is roughly a factor of two increase in the apparent wavelength of the observed disturbances, and the propagation direction of the waves is more nearly perpendicular to the jet axis. This change in propagation direction would be expected for an increase in Froude number. The local Froude number can be interpreted as the ratio of the local flow velocity to the phase velocity of waves with a wavelength comparable to the local, characteristic lengthscale of the jet. A larger Froude number, therefore, implies a larger velocity difference and, hence, more refraction. This is consistent with the result of Madnia & Bernal (1994).

Comparison of figures 2 and 3 shows that the waves propagate well beyond the region of subsurface turbulence, as marked by the dye. It also shows that above the turbulent core region in the low-Froude-number jet there are observable surface features, but that these features appear to be spatially correlated with the subsurface flow and do not represent travelling waves. The distinction between these features and the travelling waves, such as those generated by the initial interaction in both jets, is important. The travelling waves serve to radiate energy away from the flow. The other surface features identified far downstream in the low-Froude-number jet (and which will presumably exist at higher Froude number, although they may be obscured by other disturbances) do not result in waves which radiate energy away from the flow.

Shadowgraph images of select regions of the surface for the high-Reynolds-number jet are shown in figure 4. Owing to the physical size of this flow, the shadowgraphs capture only a small area of the jet ( $10d \times 10d$ ). In the figure, the perimeter line indicates a non-dimensional field of view which is the same streamwise length and half the width of that shown in figure 3(a), and the positions of the two small shadowgraph images correspond to their actual physical locations in this field. Owing to their small size, these images cannot show the travelling waves generated by this jet. However, we can see the nature of the smaller-scale surface disturbances generated by the turbulence. For this case, there are clearly more small-scale free-surface disturbances visible than for either low-Reynolds-number case. Also evident in both images are the signatures of long vortex filaments which have connected to the free surface at multiple locations. (The reconnection process is visible in the time sequence from which this image was taken.) This type of feature, which appears to be related to the vortex-pair instability of Crow (1970), has not been observed in the lower-Reynolds-number jet flows examined as part of this study, or in the investigations of Anthony & Willmarth (1992) and Madnia & Bernal (1994).

It appears that this behaviour is a significant feature of high-Reynolds-number flows. At high Reynolds number, the diffusion timescale for vorticity is longer than at low Reynolds number. For the high-Reynolds-number jet, the diffusion timescale is long enough for the Crow (1970) instability and resulting reconnection to occur. For lower-Reynolds-number flows, viscous diffusion may eliminate the near-surface, coherent tangential vorticity before this can happen. This would explain the differences in the shadowgraph images.

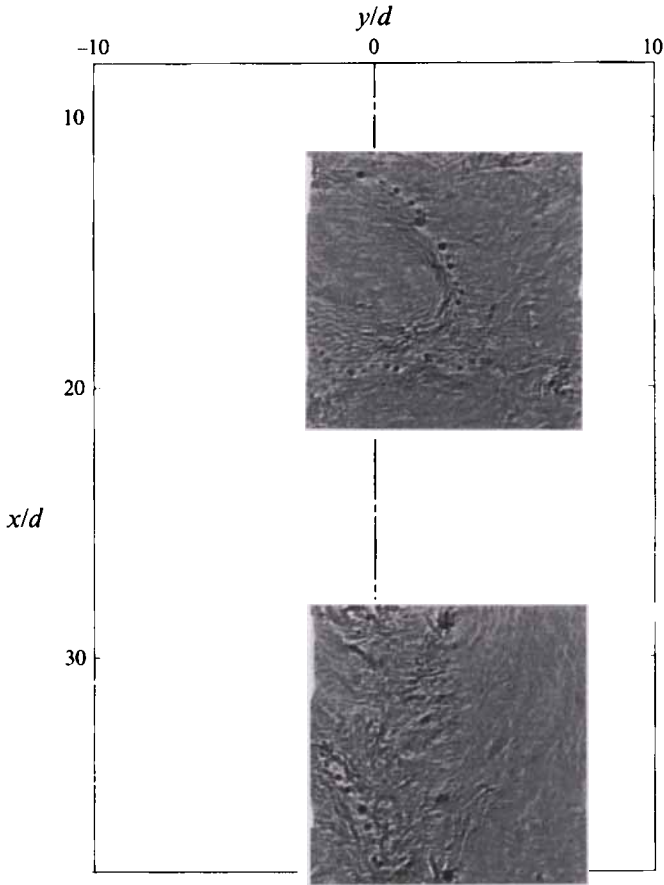


FIGURE 4. Shadowgraph visualization of the free-surface disturbances generated by the jet for  $Re = 102000$  and  $Fr = 1.0$ . The outline box represents one-half the field of view shown in figure 3(a) ( $20d$  across  $\times$   $30d$  long); each small image is  $10d \times 10d$  and is located at its appropriate position in the box. The top edge of the box corresponds to  $x/d = 8$ .

Figure 5 shows a time series of surface elevation profile above the jet axis for the high-Froude-number case ( $Fr = 8.0$ ). The upper edge of each bright region represents the free surface. The time delay between each frame is 10 ms, and the exposure time for each frame is 35  $\mu$ s. The horizontal range of this image is from  $x/d = 6$ , just before the initial interaction of the jet with the free surface, to  $x/d \approx 35$ , downstream of the second set of velocity measurements. The vertical scale of this image has not been distorted; the tick marks on the left edge of the figure are spaced one jet diameter  $d$  apart. For  $x/d = 16$  and 32 the r.m.s. surface elevation was estimated using the time series from which figure 5 was taken. The results were presented above the table 2. (For comparison, similar analysis at  $x/d = 16$  for the intermediate case,  $Fr = 1.0$ , resulted in r.m.s. surface elevation of  $0.0079d$ , nearly an order of magnitude smaller. This required video images of a region only a few jet diameters long in order to improve vertical resolution). In figure 5 we can see that the free-surface disturbances generated in the high-Froude-number flow can be extremely steep, with surface slopes approaching unity. Qualitative observations of the high-Reynolds-number case indicated that the free-surface elevations were small and similar to the intermediate case, although direct visualization was not done.

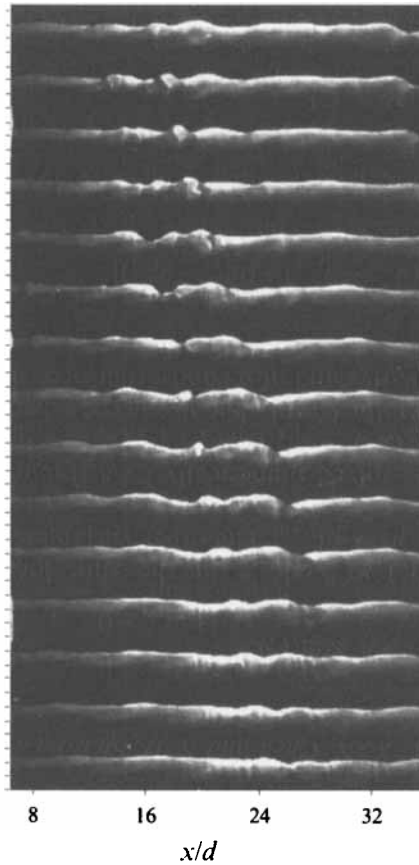


FIGURE 5. Time series of surface elevation profiles along the jet axis ( $y/x = 0$ ) showing disturbances generated by the jet for  $Re = 12700$  and  $Fr = 8.0$ . Time increases from top to bottom with 10 ms between successive images.

### 3.2. Mean velocities and related quantities

To demonstrate that the results of the present study are consistent with those of previous studies by Anthony & Willmarth (1992) and Madnia & Bernal (1994) we will compare the downstream evolution of several quantities. The results of Madnia & Bernal were obtained at a single Reynolds number and various values of  $h/d$ . To compare their results to those of the present study, a local Froude number associated with the initial interaction  $Fr_i$  is defined (in keeping with the discussion above) as

$$Fr_i = \left( \frac{U_0}{(gd)^{1/2}} \right) \left( \frac{d}{h} \right)^{3/2}.$$

The  $Fr_i$  for the results of Madnia & Bernal, Anthony & Willmarth, and the present high-Froude-number case are of the same order of magnitude ( $1.22 < Fr_i < 8.01$ ). However,  $Fr_i$  for the present low-Froude-number cases are substantially smaller than the others ( $Fr_i = 0.36$ ). The results are compared in figure 6, and the Froude and Reynolds numbers for the various data are given in the caption of the figure. These will be useful in comparing the observed behaviour for the various cases.

Figure 6 shows the downstream evolution of quantities associated with the mean and r.m.s. streamwise velocity profiles for the present study, along with those of Madnia & Bernal (1994) and Anthony & Willmarth (1992). Figure 6(a) shows the decay of the

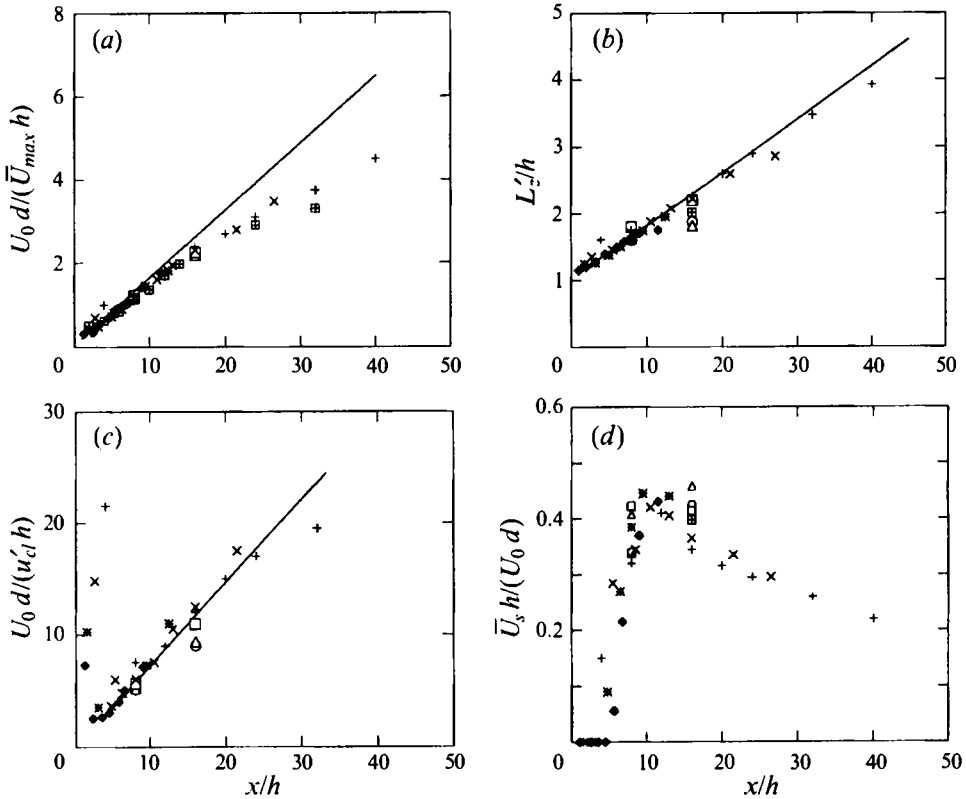


FIGURE 6. Comparison of various quantities to the results of Madnia & Bernal (1994) and Anthony & Willmarth (1992). Solid lines are least-squares fits to the free-jet data of Madnia & Bernal, downstream evolution of: (a) the maximum mean streamwise velocity  $\bar{U}_{max}$ ; (b) the characteristic lengthscale  $L'_z$ ; (c) the r.m.s. streamwise velocity on the jet axis  $u'_{cl}$ ; (d) surface mean streamwise velocity  $\bar{U}_s$ . From Madnia & Bernal (1994) for  $Re = 12700$ : +,  $Fr_i = 8.01$ ; ×,  $Fr_i = 4.36$ ; \*,  $Fr_i = 2.03$ ; ◇,  $Fr_i = 1.22$ . From Anthony & Willmarth (1992): □,  $Re = 12700$  and  $Fr_i = 2.84$ . Present study: □,  $Re = 12700$  and  $Fr_i = 2.84$  ( $Fr = 8.0$ ); △,  $Re = 12700$  and  $Fr_i = 0.36$  ( $Fr = 1.0$ ); ○,  $Re = 102000$  and  $Fr_i = 0.36$  ( $Fr = 1.0$ ).

maximum mean streamwise velocity. The present data collapse well to the data reported by Madnia & Bernal (1994) and Anthony & Willmarth (1992). The solid line represents a least-squares fit to the free-jet data. Figure 6(b) shows the downstream evolution of the characteristic lengthscale  $L'_z$  proposed by Madnia & Bernal (1994). ( $L'_z$  is defined as the distance from the free surface to the location below the jet axis where the mean streamwise velocity is half of the maximum mean streamwise velocity.) At  $x/d = 16$ , which is equivalent to  $x/h = 8$  in the figure, the present data agree with the data presented by Madnia & Bernal (1994) and Anthony & Willmarth (1992). At  $x/d = 32$  ( $x/h = 16$ ), the high-Froude-number case collapses well with the data reported by Madnia & Bernal (1994) but is greater than that of Anthony & Willmarth. The low-Froude-number cases are about 18% lower than those of Madnia & Bernal. As we will show below, the low-Froude-number jets exhibit a larger outward velocity at the free surface than the high-Froude-number case. This would result in the smaller values of  $L'_z$  observed for the low-Froude-number jets. Figure 6(c) shows the downstream evolution of the r.m.s. streamwise velocity at the jet centreline  $u'_{cl}$ . At both locations, the present data agree with the results of Anthony & Willmarth and Madnia & Bernal where the values of  $Fr_i$  are comparable. The two low-Froude-number cases

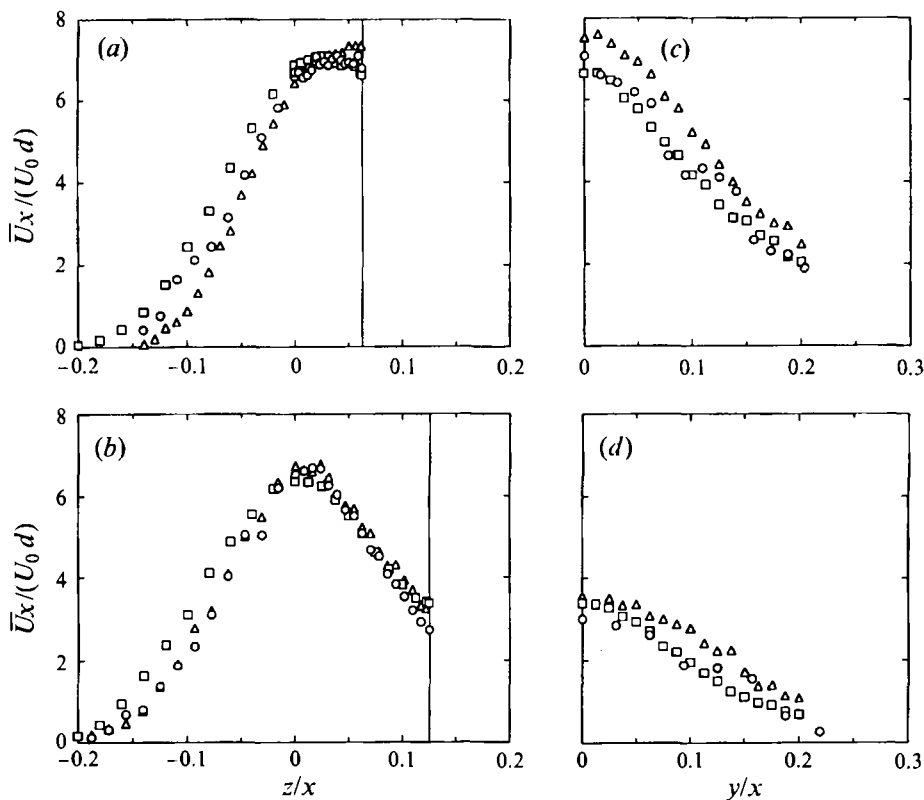


FIGURE 7. Profiles of mean streamwise velocity  $\bar{U}$ :  $\circ$ ,  $Re = 102\,000$ ,  $Fr = 1.0$ ;  $\triangle$ ,  $Re = 12\,700$ ,  $Fr = 1.0$ ;  $\square$ ,  $Re = 12\,700$ ,  $Fr = 8.0$ . Vertical profiles on the symmetry plane ( $y/x = 0$ ) for (a)  $x/d = 32$ , (b)  $x/d = 16$ . Horizontal profiles at the free surface ( $z/d \approx 2$ ) for (c)  $x/d = 32$ , (d)  $x/d = 16$ .

from the present study have higher levels of  $u'_{ci}$ . Below, we will show that the turbulence-kinetic-energy levels are lower in high-Froude-number flows owing to loss of energy from the turbulence to generation of surface waves. Figure 6(d) shows the downstream evolution of the mean streamwise velocity at the free surface  $\bar{U}_s$ . The present results are slightly higher than the data reported by Madnia & Bernal (1994) at  $x/h = 8$ . At  $x/h = 16$ , the present data agree with the data of Anthony & Willmarth for comparable Froude number, but are consistently 10% higher than those of Madnia & Bernal. The only data from Madnia & Bernal for  $x/h = 16$  are at higher Froude numbers than were examined in the present study, and so the observed difference in  $\bar{U}_s$  may be attributed to the difference in Froude number.

From the foregoing, we conclude that the data for the present study are consistent with those of both Anthony & Willmarth (1992) and Madnia & Bernal (1994) for comparable Froude numbers.

Figure 7 shows vertical and horizontal profiles of the mean streamwise velocity  $\bar{U}$  at  $x/d = 16$  and 32. Figures 7(a) and 7(b) show vertical profiles on the symmetry plane ( $y = 0$ ) for the two downstream locations. The location of the undisturbed free surface is denoted by the vertical line in the figure. With the scaling used, the effect of the free surface is evident. The distance between the jet axis and the free surface decreases, relative to the local scale of the jet, as the jet proceeds downstream. This causes the velocity to be larger at the locations near the free surface than it would be in a jet in

$Fr = \frac{U_0}{(g/d)^{1/2}}$	$Re = \frac{U_0 d}{\nu}$	$x/d$	$U_c/U_0$	$l_c/d$	$Fr_{local} = \frac{U_c}{(2gl_c)^{1/2}}$	$Re_{local} = \frac{2U_0 l_c}{\nu}$
8.0	12700	16	0.406	1.60	1.814 (0.227)	16500 (1.30)
1.0	12700	16	0.423	1.62	0.235 (0.235)	17400 (1.37)
1.0	102000	16	0.418	1.50	0.241 (0.241)	128000 (1.25)
8.0	12700	32	0.222	3.36	0.684 (0.086)	18900 (1.48)
1.0	12700	32	0.229	3.39	0.088 (0.088)	19800 (1.55)
1.0	102000	32	0.222	2.98	0.091 (0.091)	135000 (1.32)

TABLE 3. Estimates values of local characteristic length and velocity scales and resulting local Froude and Reynolds numbers for various jet flows at the downstream distances examined

an infinite medium. At  $x/d = 16$ , the velocity profiles are in good agreement for the region above the jet axis. However,  $\bar{U}$  for the low-Froude-number cases is smaller in magnitude below the jet axis. The maximum in  $\bar{U}$  occurs at  $z/x = 0$  for all cases. At  $x/d = 32$ , all the maxima have shifted toward the free surface. The maxima are at  $z/x = 0.02$  for the high-Reynolds-number and high-Froude-number cases, and the maximum occurs at the free surface for the intermediate case. Below the jet axis, the intermediate case is narrower than the other two cases.

Horizontal profiles of  $\bar{U}$  at the free surface,  $z/d \approx 2$ , are shown in figures 7(c) and 7(d). For the low-Reynolds-number cases at  $x/d = 16$  (figure 7d), the velocities agree for  $y/x < 0.06$ , but the velocity for the high-Reynolds-number case is lower. For  $y/x > 0.06$  the high-Reynolds-number and the high-Froude-number cases agree, but, the intermediate case exhibits slightly higher velocity than the other two cases. At  $x/d = 32$ , the discrepancy between the intermediate case and the other two cases extends across the entire profile, and is more pronounced.

From the vertical profiles of  $\bar{U}$  shown in figure 7(a) and 7(b) we can determine the characteristic lengthscale  $l_c$  and velocity scale  $U_c$ . In keeping with the usual practice (see, e.g. Tennekes & Lumley 1972), we take the characteristic velocity scale as the maximum velocity, and take the distance from the maximum to the point where the velocity is half the maximum velocity as the characteristic lengthscale. Since the velocity in the upper half of the jet does not drop to zero owing to the free surface, we obtain  $l_c$  from the lower half of the jet. Table 3 contains the estimated values of  $U_c$  and  $l_c$  for the three jets examined here for the two streamwise locations. For the three cases the characteristic velocity scales at a given  $x/d$ -location agree to within 5%. The characteristic lengthscales for the two low-Reynolds-number cases agree to within 2% for both  $x/d$ -locations, but  $l_c$  for the high-Reynolds-number jet is 7% lower at  $x/d = 16$  and 12% lower at  $x/d = 32$  than the low-Reynolds number jets.

Using these velocity and length scales we can estimate local values of the Froude and Reynolds numbers. These results are shown in the last two columns of table 3. (Here we use  $2l_c$  in the Froude and Reynolds number to be consistent with the use of jet diameter – rather than radius – in defining  $Fr$  and  $Re$  based on the jet-exit conditions.) The numbers in parentheses under the local Froude and Reynolds numbers are the ratios of the local values of these parameters to those defined on the basis of the jet-

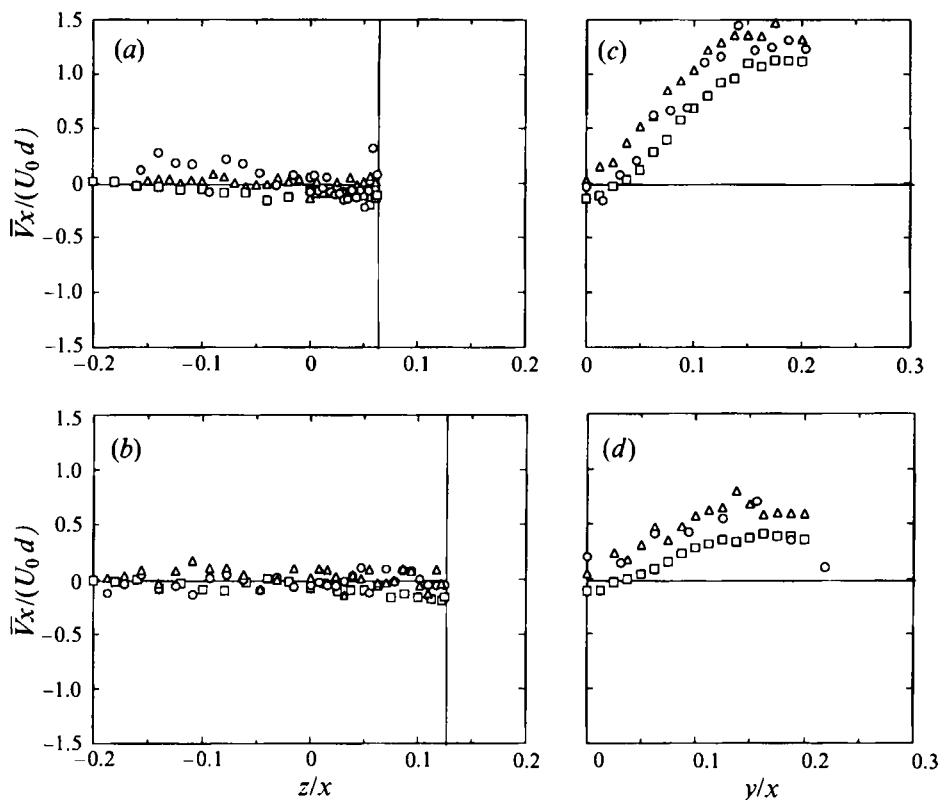


FIGURE 8. As figure 7 but profiles of mean transverse velocity  $\bar{V}$ .

exit conditions. Madnia & Bernal (1994) proposed that a free-surface jet would scale as jet in an infinite medium, but with twice the momentum flux. (The doubling of the momentum flux is due to the presence of the 'image' jet above the free surface.) This scaling implies that the local Reynolds number of the jet after it has interacted with the free surface will be larger by a factor of  $\sqrt{2}$ , a 41% increase. The results of Madnia & Bernal (1994) show an increase of 64% in the characteristic velocity for  $x/h \geq 15$  ( $x/d \geq 30$  for the present experiment). They attributed the difference to either the presence of surface-active agents, confinement effects or loss of momentum due to surface waves; however, a loss of momentum due to either the momentum flux associated with the entrained fluid or the generation of waves would result in the opposite effect (i.e. the constant  $c_1$  in equation (9) of Madnia & Bernal would increase if there was momentum loss from the jet). For  $x/d = 16$ , the local Reynolds numbers have risen by 25–37%, with the largest increase occurring for the intermediate case, followed by the high-Froude-number, low-Reynolds-number case. The high-Reynolds-number case shows the smallest increase in local Reynolds number. At  $x/d = 32$ , the Reynolds numbers for all cases have increased further, but the two low-Reynolds-number cases are more closely in agreement and the high-Reynolds-number case is significantly lower. The two low-Reynolds-number cases actually show increases of more than 41%, consistent with the results of Madnia & Bernal (1994). In these experiments, great care was taken to eliminate surfactant effects, hence the larger than expected increase in Reynolds number remains unexplained. One possibility, neglected in the model of a jet merging with its image above the free surface (which is inherently

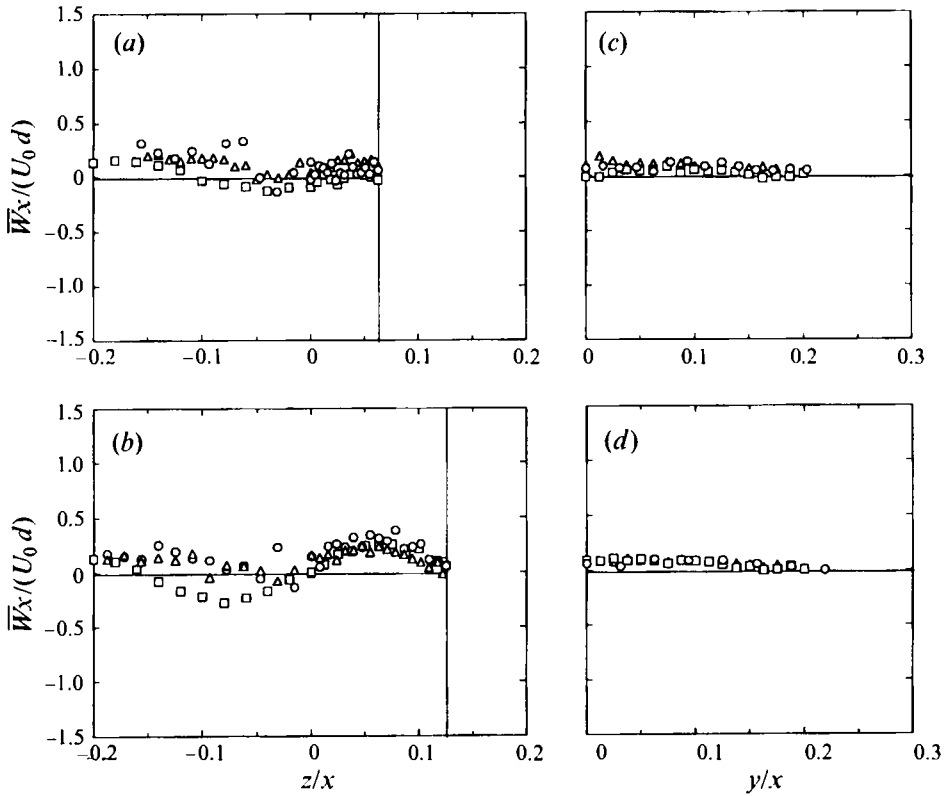


FIGURE 9. As figure 7 but profiles of mean vertical velocity  $\bar{W}$ .

a potential flow model), is the interaction of the vorticity in the jet with the free surface. This could serve either to accelerate or retard the evolution of the flow in the presence of the free surface.

As discussed in §3.1 above, the local Froude number for a jet will decrease with increasing streamwise distance. The local Froude numbers shown in table 3 for  $x/d = 16$  for the three jets examined show that the two low-Reynolds-number jets exhibit a more rapid decrease in Froude number than the high-Reynolds-number case (based on the ratio of the local Froude number to the Froude number based on jet-exit conditions for a given case). The decrease in local Froude number is slightly more rapid for the high-Froude-number jet. These results also apply at  $x/d = 32$ .

The results shown in table 3 show that for the low-Reynolds-number jets the Reynolds number increases, and the Froude number decreases, more rapidly in terms of streamwise distance. Hence, these low-Reynolds-number jets evolve more quickly in the presence of the free surface than the high-Reynolds-number jet.

Figure 8 shows vertical and horizontal profiles of the mean transverse velocity,  $\bar{V}$ . For all cases, the vertical profiles in figures 8(a) and 8(b) show a near-zero velocity, as would be expected on the symmetry plane of the jet. Horizontal profiles of  $\bar{V}$  are shown in figure 8(c) and figure 8(d). At both streamwise locations, the two low-Froude-number cases show essentially the same  $\bar{V}$  at the free surface, and the high-Froude-number jet exhibits consistently lower  $\bar{V}$ . At  $x/d = 16$ , the maximum  $\bar{V}$  is 50% larger for the low-Froude-number cases. At  $x/d = 32$ , the maximum  $\bar{V}$  for the high-Froude-number case has increased significantly and is only 20% lower than the low-Froude-number case. For all the cases  $\bar{V}$  has increased by more than 150% relative to the levels

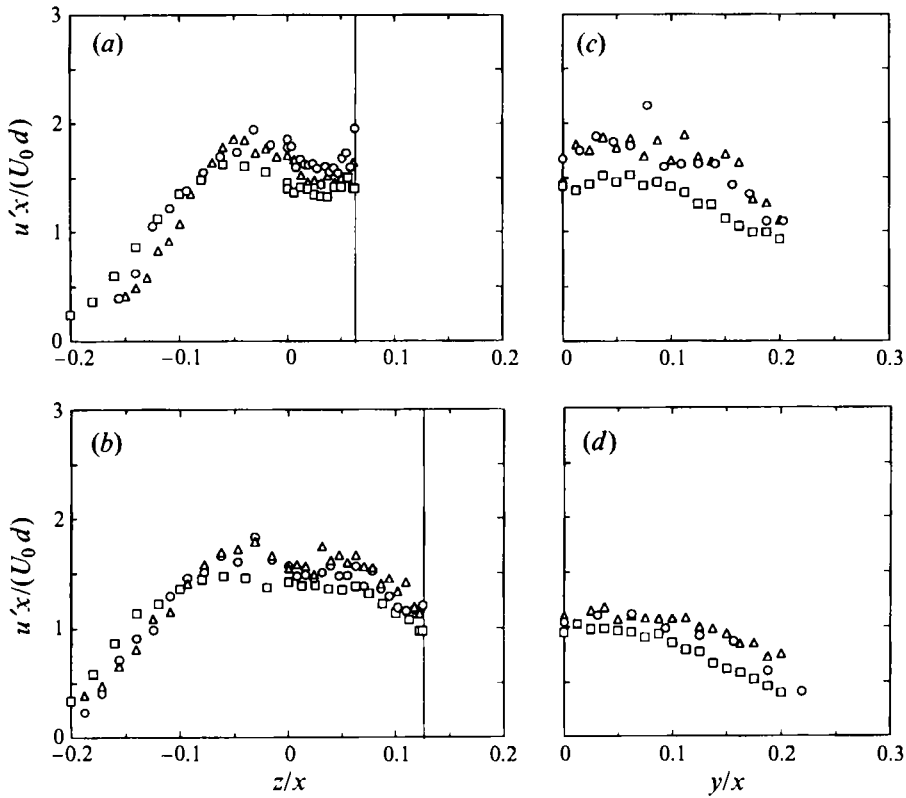


FIGURE 10. Profiles of r.m.s. streamwise velocity  $u'$ :  $\circ$ ,  $Re = 102000$ ,  $Fr = 1.0$ ;  $\triangle$ ,  $Re = 12700$ ,  $Fr = 1.0$ ;  $\square$ ,  $Re = 12700$ ,  $Fr = 8.0$ . Vertical profiles on the symmetry plane ( $y/x = 0$ ) for (a)  $x/d = 32$ , (b)  $x/d = 16$ . Horizontal profiles at the free surface ( $z/d \approx 2$ ) for (c)  $x/d = 32$ , (d)  $x/d = 16$ .

at  $x/d = 16$  (200% for the high-Froude-number case) using this scaling. These changes in  $\bar{V}$  represent physical increases in  $\bar{V}$  of 75–100% as well as the above-stated non-dimensional increases. In all cases and for both streamwise locations the maximum  $\bar{V}$  is located at  $y/x = 0.10$ – $0.15$ . Hence, the magnitude of the transverse velocities are Reynolds-number independent and decrease with increasing Froude number; however, the Froude-number-related differences lessen with increasing streamwise distance.

Profiles of the mean vertical velocity  $\bar{W}$  are shown in figure 9. Vertical profiles of  $\bar{W}$  on the symmetry plane at  $x/d = 16$  are shown in figure 9(b). For all cases,  $\bar{W}$  is consistently positive above the jet axis ( $z/x > 0$ ) and far below the jet axis, in the entrainment field of the jet ( $z/x < -0.15$ ). For the high-Froude-number case, immediately below the jet axis  $\bar{W}$  is negative due to the spreading which occurs in the core of the jet (Wynanski & Fiedler 1969). For the two low-Froude-number cases,  $\bar{W}$  is uniformly positive below the jet axis except for possibly a small region immediately below the jet axis. This is consistent with the narrower  $\bar{U}$ -profiles below the jet axis of the two low-Froude-number cases, as well as the stronger outward flow at the surface (figure 8d). Vertical profiles of  $\bar{W}$  at  $x/d = 32$  are shown in figure 9(a). The two low-Froude-number cases are similar to those at  $x/d = 16$  for  $z < 0$ . However, above the jet axis, the upward velocity is smaller in magnitude. This indicates that the strong outward flow at the surface which is still in evidence at  $x/d = 32$  (figure 8c) is driven either by upwelling in regions removed from the jet axis, or by a decrease in the

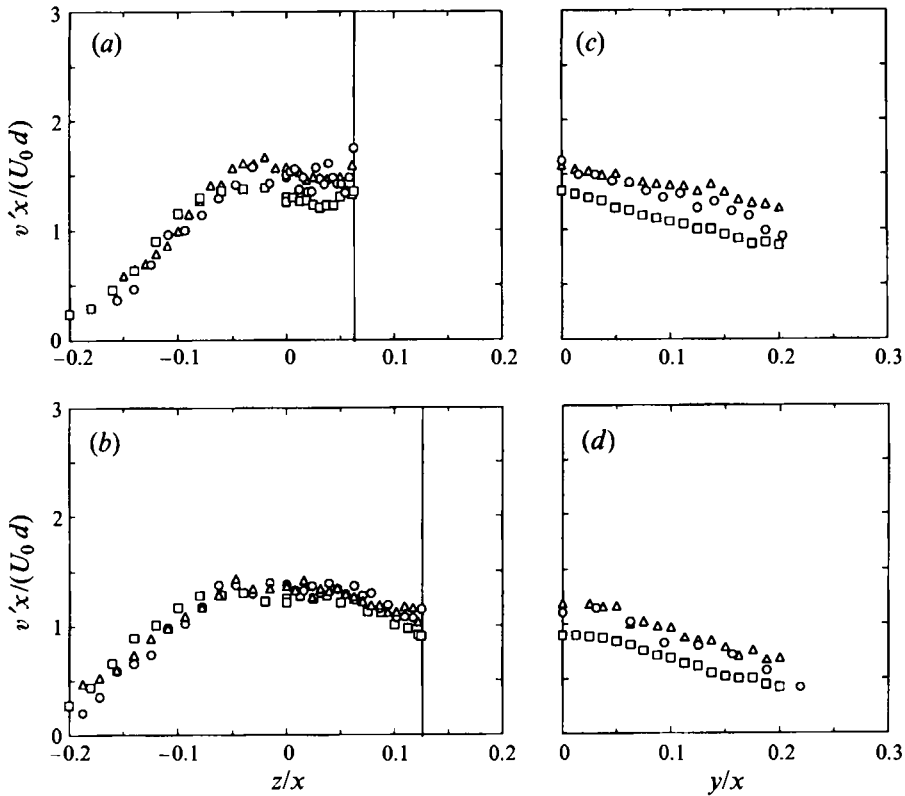


FIGURE 11. As figure 10 but profiles of r.m.s. transverse velocity  $v'$ .

streamwise velocity. These results show that with increasing streamwise distance, the vertical velocity profiles are tending to a uniform positive  $\bar{W}$  over depth. The low-Froude-number cases are approaching this state more rapidly than the high-Froude-number jet. The horizontal profiles of  $\bar{W}$  at  $x/d = 16$  and  $32$  (figures 9c and 9d) show that the upward flow is small near the free surface for all cases.

### 3.3. Reynolds stresses and related quantities

In this section, statistical quantities associated with the turbulent stresses are examined. These include the root-mean-square (r.m.s.) velocities (i.e. the square-roots of the Reynolds normal stresses), the turbulence kinetic energy and the Reynolds shear stresses and quantities derived from them.

Profiles of the r.m.s. streamwise velocity  $u'$  for  $x/d = 16$  and  $32$  are shown in figure 10 for the three sets of conditions. Overall, the results from the two low-Froude-number cases are in agreement, but the high-Froude-number case shows a consistent 10–20% deficit in  $u'$  for roughly  $z/x > -0.1$  and a consistently larger  $u'$  for  $z/x < -0.1$  for  $x/d = 16$  and  $32$ . The slight excess in  $u'$  for  $z/x < -0.1$  is consistent with the larger vertical width for the high-Froude-number jet seen in the mean streamwise velocity profiles (figure 7). A deficit in  $u'$  for  $Fr = 8.0$  is also observed in the horizontal profiles at the free surface, shown in figures 10(c) and 10(d). At  $x/d = 16$ , the difference in  $u'$  for the high-Froude-number case and the other two low-Froude-number cases is more pronounced for  $y/x > 0.1$  outside the active wave-making region above the core of the jet. At  $x/d = 32$ , this difference is almost uniform across the horizontal profile.

Corresponding profiles of the r.m.s. transverse velocities  $v'$  are shown in figure 11.

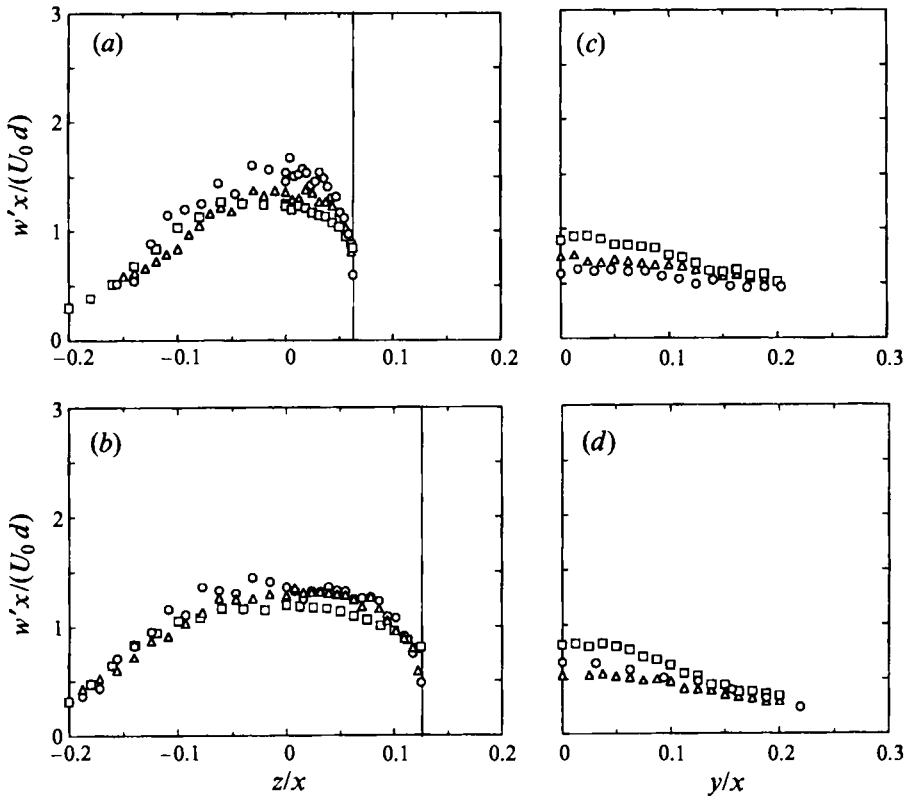


FIGURE 12. As figure 10 but profiles of r.m.s. vertical velocity  $w'$ .

In general, the levels of  $v'$  are about 20% lower than  $u'$ . This anisotropy is as expected for a shear flow. At  $x/d = 16$ , shown in figures 11(b) and 11(d), the behaviour is generally similar to that exhibited by  $u'$ , except that for the high-Froude-number case  $v'$  is lower near the free surface. The differences in  $v'$  are very small for  $z/x > -0.1$  in the vertical profiles, but near the free surface,  $v'$  for the high-Froude-number case is about 20% lower than that for the low-Froude-number cases. Further downstream, at  $x/d = 32$  (figures 11a and 11c), the two low-Froude-number cases are in agreement and the high-Froude-number flow exhibits approximately 10% lower  $v'$  for  $z/x > -0.05$ . Horizontal profiles of  $v'$ , shown in figures 11(c) and 11(d) indicate that for the high-Froude-number case,  $v'$  is consistently 10–20% lower than for the other cases.

In figure 12 are shown vertical and horizontal profiles of the r.m.s. vertical velocity  $w'$  at  $x/d = 16$  and 32. For the vertical profiles at  $x/d = 16$ , the behaviour of  $w'$  for  $z/x < 0.1$  is very similar to the results for  $v'$  shown in figure 11(b). For  $z/x > 0.1$ ,  $w'$  rapidly decreases as the free surface is approached for the low-Froude-number cases. The level of  $w'$  for the low-Froude-number cases is about 30–40% lower than the high-Froude-number case at the free surface. In horizontal profiles at the free surface for  $x/d = 16$  (figure 12d), the high-Froude-number case shows a consistently elevated  $w'$  level for  $y/x < 0.1$ , relative to the low-Froude-number cases. This region corresponds to the portion of the free surface directly above the core of the jet and the increased  $w'$  is consistent with the more pronounced wave generation which occurs in this case. But for  $y/x > 0.1$ , the  $w'$  levels for all cases are essentially identical. At  $x/d = 32$  (figure 12c), similar results are seen except that the Froude-number-related differences in  $w'$  are smaller. Near the free surface at  $x/d = 32$ , the levels of  $w'$  are reduced relative to

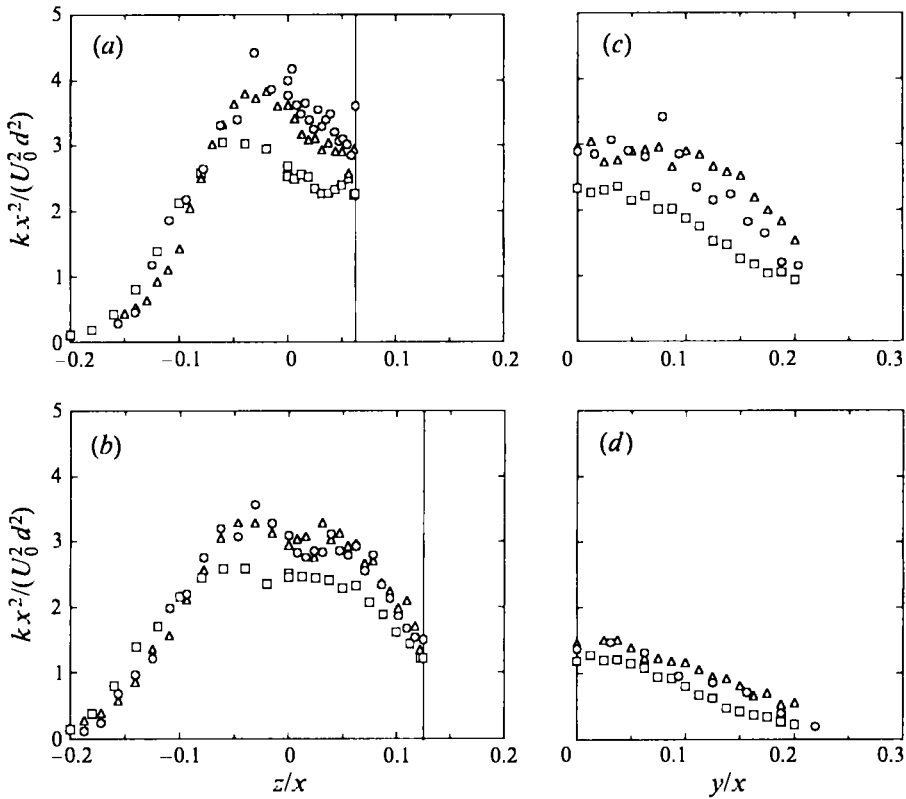


FIGURE 13. Profiles of turbulence kinetic energy  $k$ :  $\circ$ ,  $Re = 102000$ ,  $Fr = 1.0$ ;  $\triangle$ ,  $Re = 12700$ ,  $Fr = 1.0$ ;  $\square$ ,  $Re = 12700$ ,  $Fr = 8.0$ . Vertical profiles on the symmetry plane ( $y/x = 0$ ) for (a)  $x/d = 32$ , (b)  $x/d = 16$ . Horizontal profiles at the free surface ( $z/d \approx 2$ ) for (c)  $x/d = 32$ , (d)  $x/d = 16$ .

$u'$  and  $v'$ , for all cases. This is consistent with the general decrease in local Froude number with increasing streamwise distance.

Profiles of turbulence kinetic energy  $k = \frac{1}{2}\overline{u_i u_i}$  are shown in figure 13. At  $x/d = 16$ ,  $k$  for the high-Froude number case is lower than that for low-Froude-number cases for  $z/x > -0.1$ . This indicates that more energy is transferred from the subsurface flow to the wave field in the high-Froude-number case. Since the local Froude number for the two low-Froude-number cases is small, there is not much energy transferred to the surface wave field. At  $x/d = 32$ , the difference in  $k$  between high- and low-Froude-number cases is somewhat larger than that at  $x/d = 16$ . This is consistent with the occurrence of wave generation beyond  $x/d = 16$ . This is consistent with the occurrence of wave generation beyond  $x/d = 16$  in the high-Froude-number case (figure 3b).

One striking feature of figures 10, 11, and 12 is the difference in r.m.s. levels at the free surface for the high- versus low-Froude-number cases, particularly at  $x/d = 16$ . For the low-Froude-number cases, the tangential velocity fluctuations are increased compared to the high-Froude-number case, and the vertical fluctuations are reduced by 30–40%. As a result, the turbulence in the low-Froude-number jets is much more anisotropic at the free surface. For these cases the free surface behaves much more like a flat, shear-free boundary and, hence, vertical momentum is deflected in the horizontal direction by the free surface. This results in a reduction in  $w'$  and an increase in  $u'$  and

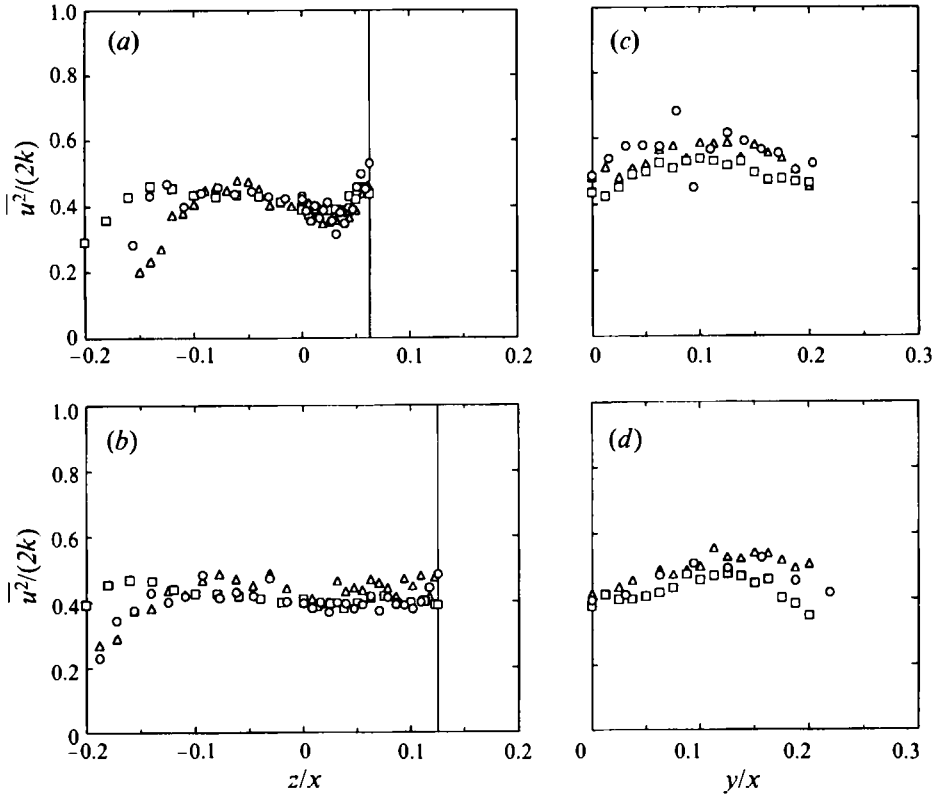


FIGURE 14. Profiles of  $\overline{u^2}/2k$ :  $\circ$ ,  $Re = 102\,000$ ,  $Fr = 1.0$ ;  $\triangle$ ,  $Re = 12\,700$ ,  $Fr = 1.0$ ;  $\square$ ,  $Re = 12\,700$ ,  $Fr = 8.0$ . Vertical profiles on the symmetry plane ( $y/x = 0$ ) for (a)  $x/d = 32$ , (b)  $x/d = 16$ . Horizontal profiles at the free surface ( $z/d \approx 2$ ) for (c)  $x/d = 32$ , (d)  $x/d = 16$ .

$v'$ . Since the local Froude number of the turbulent jets decreases with downstream distance, the behaviour of the low- and high-Froude-number cases should be more alike at  $x/d = 32$  than at  $x/d = 16$ , as shown in the results.

To quantify the relationships between the r.m.s. velocities in a more concrete fashion, we can examine how the turbulence kinetic energy is partitioned among the three velocity components. To this end, we can examine the fraction of the turbulence kinetic energy which resides in a given component of the normal Reynolds stress,  $\overline{u_i u_i}/2k$  (with no sum on  $i$ ). By definition, then,  $0 \leq \overline{u_i u_i}/2k \leq 1$  with  $\overline{u_i u_i}/2k = 1/3$  corresponding to the case of homogeneous isotropic turbulence. For a jet far removed from a free surface,  $\overline{u^2}/2k$  will generally be larger than  $1/3$ , since turbulence kinetic energy is produced in the streamwise velocity fluctuations and is then transferred to fluctuations in the other velocity components through the pressure field. For this reason,  $\overline{v^2}/2k$  and  $\overline{w^2}/2k$  will generally be less than  $1/3$ . This general behaviour will, of course, be modified near the free surface.

Figure 14 shows profiles of  $\overline{u^2}/2k$ . In the vertical profiles at  $x/d = 16$  and  $32$  (figures 14a and 14b), we see  $\overline{u^2}/2k = 0.4\text{--}0.5$  for  $z/x > -0.1$ , except for the region very near the free surface. The region for  $z/x < -0.1$  is the intermittent part of the jet and below that is the entrainment field of the jet. At  $x/d = 16$ , the high-Froude-number case shows a larger fraction of  $k$  in the  $u$ -fluctuations than the two low-Froude-number cases for  $z/x < -0.1$ . This is due to the greater width of the high-Froude-number jet in the vertical direction seen in the mean and r.m.s. velocity profiles and the lower

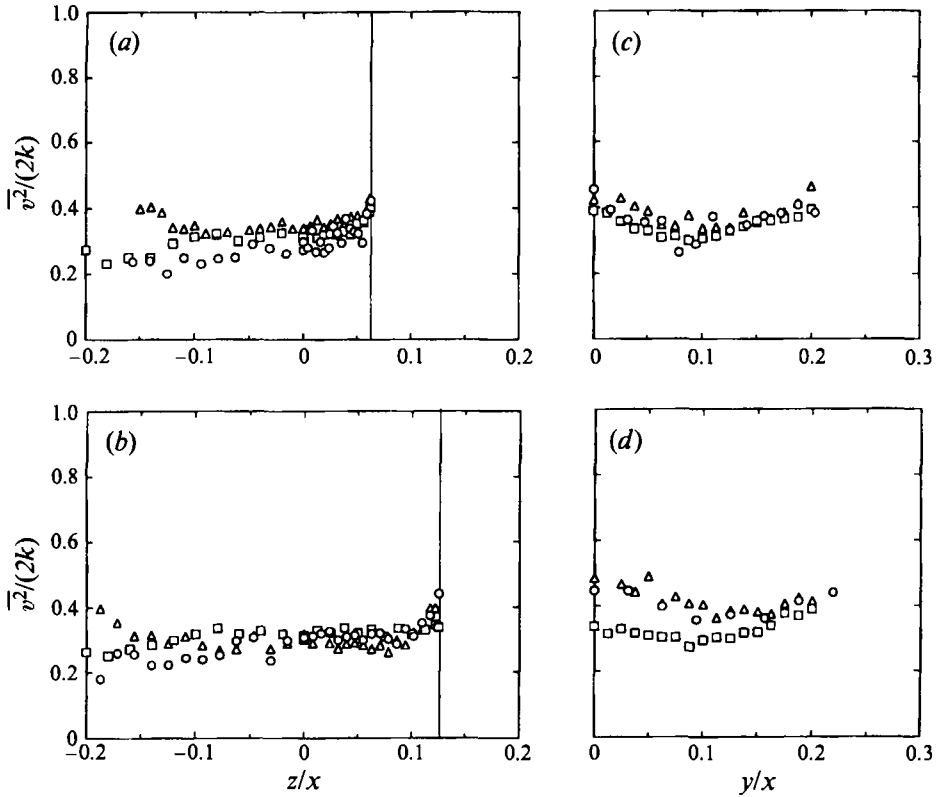
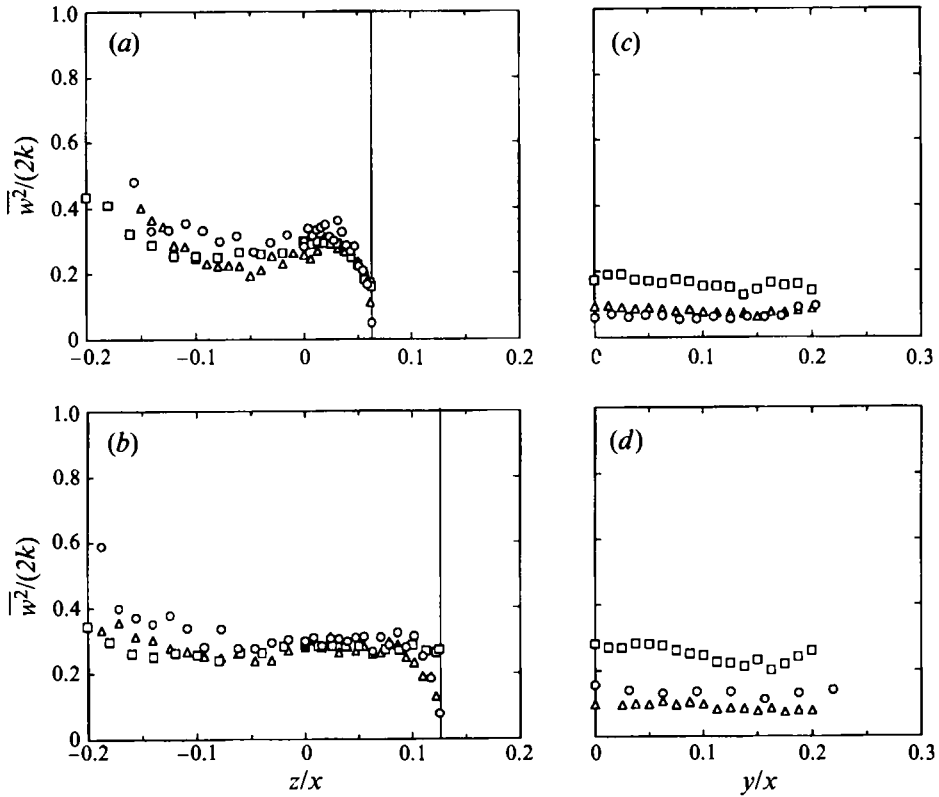


FIGURE 15. As figure 14 but profiles of  $\overline{v^2}/2k$ .

turbulence kinetic energy. At  $x/d = 32$ ,  $\overline{u^2}/2k$  is similar to that at  $x/d = 16$  for  $z/x < -0.1$ . Near the free surface, there is an increase in  $\overline{u^2}/2k$  particularly at  $x/d = 32$ , which shows that the fraction of  $k$  contained in  $u$ -fluctuations from the low-Froude-number cases is increased at the free surface relative to the level in the bulk of the flow. The horizontal profiles at the free surface (figures 14c and 14d) show that for the high-Froude-number flow at  $x/d = 16$ ,  $\overline{u^2}/2k$  does not deviate much from the other two cases for  $y/x < 0.1$ ; however, it decreases for  $y/x > 0.1$  at high Froude number. At  $x/d = 32$ , the results for the high-Froude-number case are slightly lower than for the low-Froude-number cases.

Profiles of the fraction of  $k$  represented by the  $\overline{v^2}$  Reynolds stress,  $\overline{v^2}/2k$ , are presented in figure 15. As expected,  $\overline{v^2}/2k$  is lower than  $\overline{u^2}/2k$  over most of the vertical extent of the flow, as shown in figures 15(a) and 15(b). Near the free surface,  $\overline{v^2}/2k$  on the symmetry plane ( $y = 0$ ) increases for the two low-Froude-number flows at both streamwise locations. The high-Froude-number case exhibits nearly constant  $\overline{v^2}/2k$  up to the free surface at  $x/d = 16$ , but at  $x/d = 32$  the behaviour is the same as the other cases, showing a rise in  $\overline{v^2}/2k$  near the surface. For horizontal profiles at  $x/d = 16$ , the increase in  $\overline{v^2}/2k$  at the surface for low Froude number is confined to the region above the core of the jet,  $y/x < 0.10$ . For  $y/x > 0.10$ ,  $\overline{v^2}/2k$  for the high-Froude-number jet increases until it is comparable to the levels seen in the two low-Froude-number cases. For  $x/d = 32$  there is a maximum in  $\overline{v^2}/2k$  above the jet axis, and it decreases monotonically outward to the edge of the turbulent core of the jet ( $y/x = 0.1$ ). For  $y/x > 0.1$  the fraction of  $k$  in the  $v$ -fluctuations increases.

FIGURE 16. As figure 14 but profiles of  $\overline{w^2}$ .

The fraction of  $k$  represented  $\overline{w^2}$  is shown in figure 16. Again,  $\overline{w^2}/2k$  is slightly less than  $\overline{u^2}/2k$  and increases for  $z/x < -0.1$  for all three cases, especially for  $x/d = 32$ . For locations near the free surface at  $x/d = 16$ ,  $\overline{w^2}/2k$  drops dramatically for the low-Froude-number cases – approaching the lower limit  $\overline{w^2}/2k = 0$ . The high-Froude-number case is virtually unchanged near the free surface. The differences due to Froude number are readily apparent in the horizontal profiles, figure 16(c) and 16(d). At  $x/d = 16$ ,  $\overline{w^2}/2k$  for the high-Froude-number case is roughly three times that of two low-Froude-number cases, while at  $x/d = 32$  it is more than double the low-Froude-number results. This larger level of  $\overline{w^2}/2k$  is associated with the increase in free-surface disturbances in the high-Froude-number case, but it is not clear whether it is due to turbulence driving the free surface up and down (and generating waves), or waves generated elsewhere propagating past the location in question. The loss of turbulence kinetic energy seen in the high-Froude-number jet indicates that some significant fraction of  $\overline{w^2}/2k$  at the surface results from the turbulent motions beneath the free surface (and results in wave generation). At  $x/d = 32$ , the fraction of  $k$  in the  $w$ -fluctuations for all cases near the free surface is lower than at  $x/d = 16$ ; however, the high-Froude-number results are closer to the low-Froude-number results. This is due to the general decrease in local Froude number with increasing streamwise distance, and the resulting increase in the resistance of the free surface to deflections. For this reason, all free-surface jets will approach the same zero-Froude-number limit for sufficiently large streamwise distances.

In both the horizontal and vertical profiles,  $\overline{u^2}/2k$  decreases outside of the turbulent core of the jet ( $y/x > 0.1$ ,  $z/x < -0.1$ ). In the vertical profiles, there is a corresponding

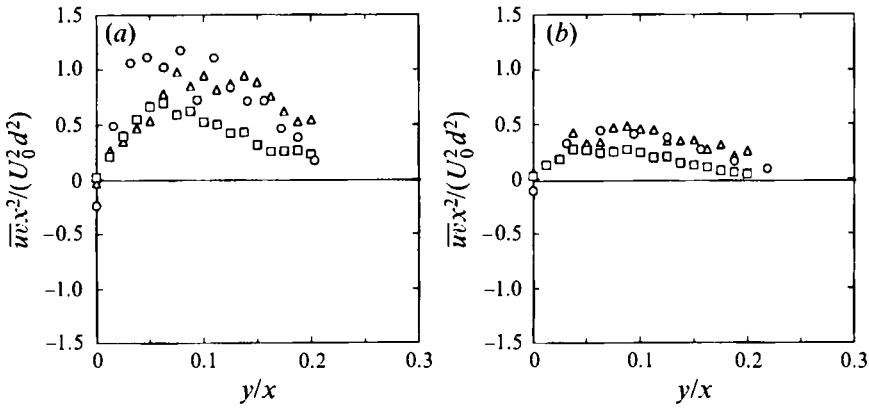


FIGURE 17. Horizontal profiles of the  $\overline{uw}$  Reynolds stress at the free surface ( $z/d \approx 2$ ) for (a)  $x/d = 32$ , (b)  $x/d = 16$ :  $\circ$ ,  $Re = 102\,000$ ,  $Fr = 1.0$ ;  $\triangle$ ,  $Re = 12\,700$ ,  $Fr = 1.0$ ;  $\square$ ,  $Re = 12\,700$ ,  $Fr = 8.0$ .

increase in  $\overline{w^2}/2k$  in this region, indicating that at the outer edges of the jet, more energy is contained in the radial velocity fluctuations associated with the entrainment and in the core of the jet there is more energy in the streamwise fluctuations. The transverse (azimuthal) velocity fluctuations remain largely unchanged. These relationships are also seen in the horizontal profiles near the free surface. For  $y/x > 0.1$ ,  $\overline{u^2}/2k$  decreases and  $\overline{v^2}/2k$  rises while  $\overline{w^2}/2k$  is relatively constant. Hence we can conclude that the variations in  $\overline{u^2}/2k$  and  $\overline{v^2}/2k$  seen in the plane of the free surface are not caused by the free surface itself. However, the Froude-number-related differences (particularly for  $y/x < 0.1$ ) are due to the free surface.

Horizontal profiles of the  $\overline{uw}$  Reynolds stress in the plane of the free surface are shown in figure 17. (On the symmetry plane, since there is no cross-stream momentum transport, the values of  $\overline{uw}$  are zero.) The profiles of  $\overline{uw}$  for  $x/d = 16$  and  $32$ , figures 17(a) and 17(b), show that the two low-Froude-number cases exhibit similar shear stress, but that for the high-Froude-number case is lower, especially for  $y/x > 0.05$ . This is related to the loss of turbulence kinetic energy in the high-Froude-number case, and is discussed below.

The  $\overline{vw}$  Reynolds stress is zero, both on the symmetry plane ( $y = 0$ ) and at the free surface ( $z \approx 2d$ ), and so is not presented here.

Vertical profiles of  $\overline{uw}$  are shown in figures 18(a) and 18(b). Generally, these profiles correspond to expectations based on the behaviour of the mean velocity profiles. The most obvious feature of the vertical  $\overline{uw}$  profiles is that the maximum which exists between the jet axis and the free surface at  $x/d = 16$  vanishes at  $x/d = 32$ . This results from the acceleration of the near-surface fluid and the resulting decrease in mean shear in this region. Also, for the high-Froude-number flow,  $\overline{uw}$  for  $z/x > -0.1$  is lower than for the other two cases, particularly for  $x/d = 16$  (figure 18b).

The relationship between the fluctuation levels for two velocities and the resulting Reynolds shear stress can be examined using the correlation coefficient

$$R_{ij} = \overline{u_i u_j} / \overline{u_i'} \overline{u_j'}$$

$R_{ij}$  can take any value between  $-1$  and  $1$ . This coefficient can be thought of as the efficiency with which turbulent velocity fluctuations transport momentum.  $R_{ij} = 0$  indicates that the velocity fluctuations are uncorrelated and no momentum transport occurs.  $R_{ij} = \pm 1$  means that the fluctuations are perfectly correlated (or anti-correlated) and the maximum level of momentum transport occurs.

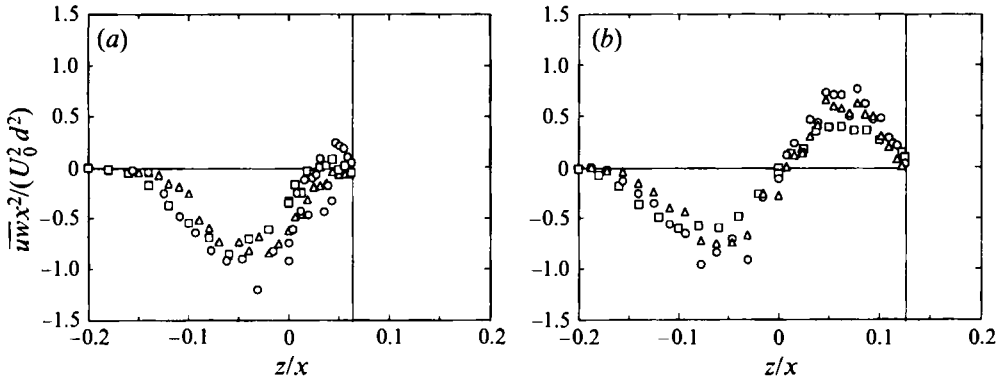


FIGURE 18. Vertical profiles of the  $\overline{uw}$  Reynolds stress on the symmetry plane for ( $y/x = 0$ ) for (a)  $x/d = 32$ , (b)  $x/d = 16$ . Symbols as figure 17.

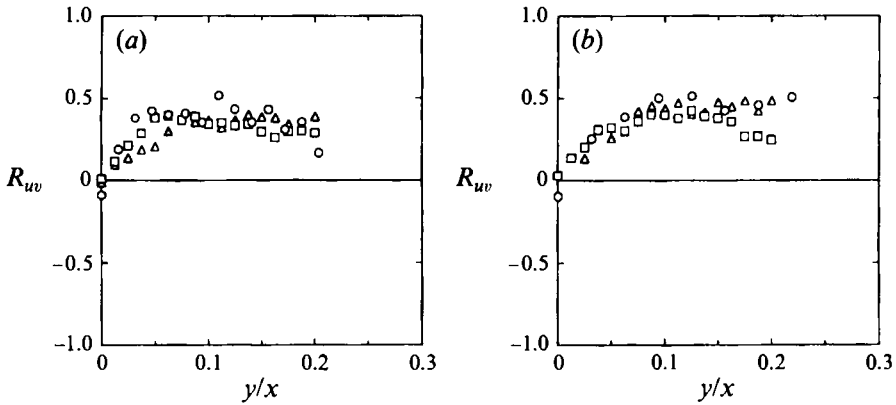


FIGURE 19. Horizontal profiles of  $R_{uv}$ , the correlation coefficient for the  $\overline{uw}$  Reynolds stress at the free surface ( $z/d \approx 2$ ) for (a)  $x/d = 32$ , (b)  $x/d = 16$ :  $\circ$ ,  $Re = 102000$ ,  $Fr = 1.0$ ;  $\triangle$ ,  $Re = 12700$ ,  $Fr = 1.0$ ;  $\square$ ,  $Re = 12700$ ,  $Fr = 8.0$ .

Correlation coefficients for the  $u$ - and  $v$ -fluctuations  $R_{uv}$  are shown in figure 19. At both locations, the results are in general agreement for all the cases except that the high-Froude-number case is a bit low for  $y/x > 0.15$  at  $x/d = 16$ . The high-Froude-number case, which exhibited lower levels of  $\overline{uw}$  (figures 17a and 17b) relative to the others has a comparable correlation coefficient level. This indicates that the lower levels of  $\overline{uw}$  for this case result directly from the low  $u'$  and  $v'$  levels (figures 10 and 11) and not from any decreased correlation in the turbulent fluctuations of  $u$  and  $v$ .

Figure 20 shows correlation coefficients for the  $\overline{uw}$  Reynolds stress  $R_{uw}$ . For  $x/d = 16$ , where  $\overline{uw}$  was lower for the high-Froude-number jet,  $R_{uw}$  is similar to the two low-Froude-number cases. This again shows that the reduced level of the Reynolds shear stress for the high-Froude-number jet is due to the reduced level of the velocity fluctuations.

### 3.4. Discussion of results

Dye visualization showed that downstream of where the jet first interacts with the free surface, a thin layer formed near the surface in which the flow diverged away from the jet axis. This was first identified in turbulent free-surface jets by Anthony & Willmarth

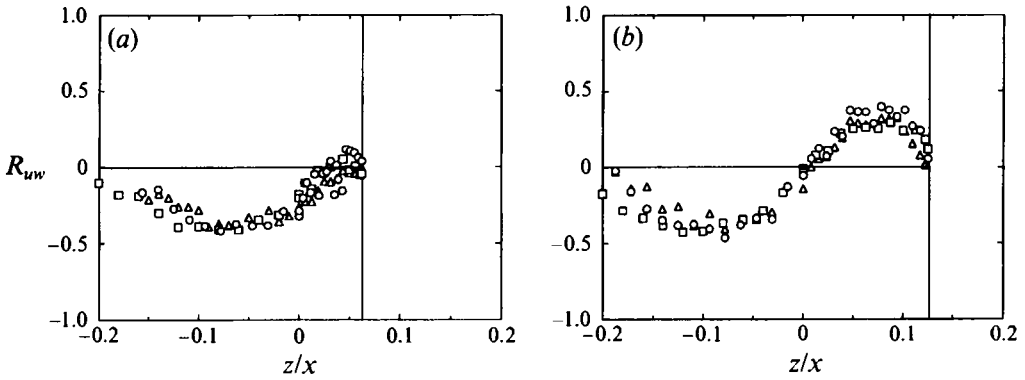


FIGURE 20. Vertical profiles of  $R_{uw}$ , the correlation coefficient for the  $\overline{uw}$  Reynolds stress on the symmetry plane for ( $y/x = 0$ ) for (a)  $x/d = 32$ , (b)  $x/d = 16$ . Symbols as figure 19.

(1992). The thin surface layer appeared to spread due to the interaction of streamwise vorticity (or the streamwise component of the instantaneous vorticity vector) with the free surface. The interaction could be described as mutual induction between the vorticity in question and its 'image' in the free surface. One obvious question is: how does this type of interaction between the turbulent vorticity field and the free surface manifest itself in the measurements of turbulent structure?

To address this, we start with the Reynolds-averaged form of the Navier–Stokes momentum equations. For free turbulent shear flows at large Reynolds number, the viscous stresses are negligible (Hinze 1975, p. 492) and so these equations reduce to

$$\frac{D\bar{U}_i}{Dt} = -\frac{1}{\rho} \frac{\partial \bar{P}}{\partial x_i} - \frac{\partial \overline{u_j u_i}}{\partial x_j}. \quad (1)$$

The surface-normal ( $z$ -direction) component of the momentum equation is

$$\frac{D\bar{W}}{Dt} = -\frac{1}{\rho} \frac{\partial \bar{P}}{\partial z} - \frac{\partial \overline{uw}}{\partial x} - \frac{\partial \overline{vw}}{\partial y} - \frac{\partial \overline{w^2}}{\partial z}. \quad (2)$$

Since changes in the streamwise direction are small, we can neglect the term involving the  $\overline{uw}$  Reynolds stress (Hinze 1975, p. 492). (This is also supported by the results presented above which show that the term involving  $\overline{uw}$  is an order of magnitude smaller than the term involving  $\overline{w^2}$ .) The results of Anthony & Willmarth (1992) showed that the  $\overline{vw}$  Reynolds stress is also small in free-surface jets (i.e.  $v$  and  $w$  are only weakly correlated, at most). The  $z$ -momentum equation is therefore well approximated by

$$\frac{D\bar{W}}{Dt} = -\frac{1}{\rho} \frac{\partial \bar{P}}{\partial z} - \frac{\partial \overline{w^2}}{\partial z}. \quad (3)$$

One of the main effects of the free surface is to cause a reduction in the  $\overline{w^2}$  Reynolds stress near the surface. We can examine this by writing the Reynolds-stress term from (1) in rotational form (Hinze 1975, p. 568):

$$\frac{\partial \overline{u_j u_i}}{\partial x_j} = \frac{\partial}{\partial x} \frac{\overline{u_i u_j}}{2} - \epsilon_{ijk} \overline{u_j \omega_k} = \frac{\partial}{\partial x_i} \overline{u_j \omega_k} - \epsilon_{ijk} \overline{u_j \omega_k}, \quad (4)$$

where  $\omega_i$  is the fluctuating vorticity ( $\epsilon_{ijk}$  is the alternating unit tensor, used to form the

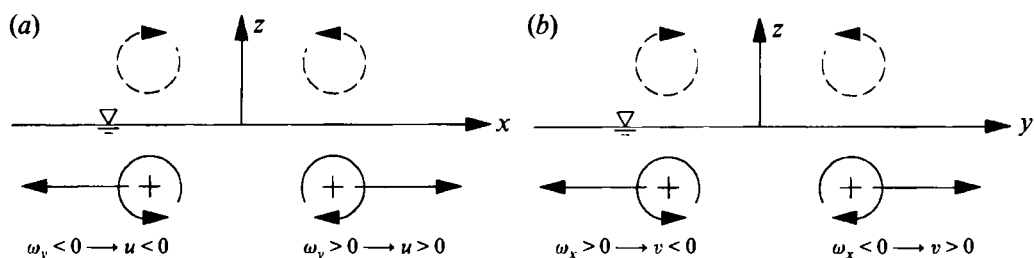


FIGURE 21. Schematics of the interaction of tangential vorticity with the free surface: (a) interaction of  $\pm\omega_y$  with the surface showing  $\overline{u\omega_y} > 0$ ; (b) interaction of  $\pm\omega_x$  with the surface showing  $\overline{v\omega_x} < 0$ .

vector cross-product between the fluctuating velocity and vorticity). If we use the same reasoning used to arrive at (3), then for the surface-normal ( $z$ -direction) component of the momentum equation, (4) becomes, to a similarly good approximation,

$$\frac{\partial}{\partial z} \overline{w^2} = \frac{\partial}{\partial z} k - (\overline{u\omega_y} - \overline{v\omega_x}). \quad (5)$$

Based on (5) we can see that the gradient in  $\overline{w^2}$  equals the gradient in the turbulence kinetic energy  $k$ , minus a contribution from the correlation of the orthogonal components of the fluctuating tangential velocities and vorticities,  $\overline{u\omega_y}$  and  $\overline{v\omega_x}$ .

To interpret these velocity–vorticity correlations, we examine a vortical element as it approaches a free surface. As the vortical element approaches a free surface, the element will move in the direction indicated by the vector cross-product  $\omega \times \hat{n}$ , where  $\hat{n}$  is the outward-pointing normal unit vector on the free surface. For a flat horizontal free surface, the behaviour will be as indicated in figure 21. For a vortex with purely  $y$ -direction vorticity ( $\omega_y$ ), the vortex will develop an  $x$ -direction velocity as it approaches the free surface. For  $\omega_y > 0$ ,  $u > 0$  and for  $\omega_y < 0$ ,  $u < 0$  (see figure 21 *a*). As a result, near the free surface  $\overline{u\omega_y}$  will be positive. Similarly for  $\omega_x > 0$ ,  $v < 0$  and vice versa (see figure 21 *b*) so  $\overline{v\omega_x}$  will be negative. This behaviour will cause the entire velocity–vorticity correlation term in (5) to be positive near a flat horizontal free surface. The interaction, then, of the turbulent vorticity field with the free surface will cause a negative gradient in  $\overline{w^2}$ . (It should be noted that as the vortical element approaches the free surface, it will take a finite amount of time to accelerate the fluid in the plane of the free surface. Further, the vortical element could have a substantial instantaneous velocity in the plane of the free surface which is in the opposite direction to that caused by the interaction of the vorticity with the free surface. In this case, the interaction will not result in a positive correlation, just a less negative one. Hence, the velocity–vorticity correlations will tend to be positive, but are not required to be.)

The energy lost from the  $w^2$  fluctuations due to the interaction of vorticity with the free surface must appear elsewhere. Using the definition of  $k$ , we can write (5) as

$$\frac{\partial}{\partial z} (\overline{u^2} + \overline{v^2}) = \frac{\partial}{\partial z} k + (\overline{u\omega_y} - \overline{v\omega_x}). \quad (6)$$

This shows that the energy which is lost from  $\overline{w^2}$  appears in the other two Reynolds normal stresses. Hence, the vorticity/free-surface interaction serves to redistribute the energy from the surface-normal to tangential velocity fluctuations.

We can use the data presented above to get an indication of the role of the

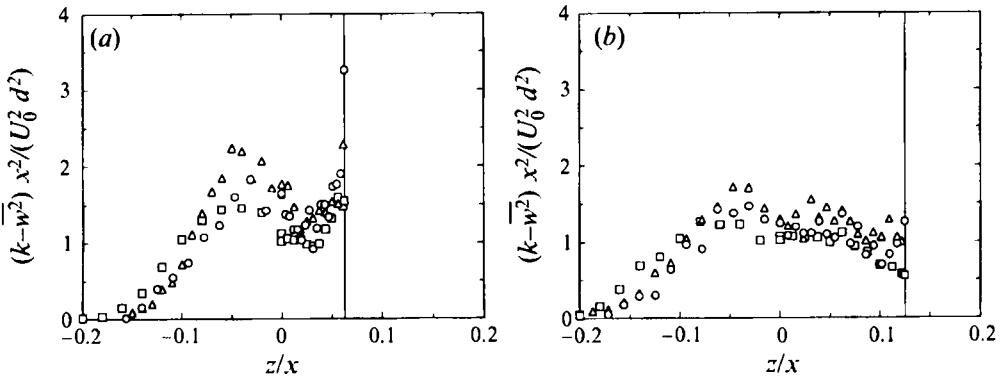


FIGURE 22. Vertical profiles of  $k - \overline{w^2}$  on the symmetry plane ( $y/x = 0$ ) for (a)  $x/d = 32$ , (b)  $x/d = 16$ :  $\circ$ ,  $Re = 102000$ ,  $Fr = 1.0$ ;  $\triangle$ ,  $Re = 12700$ ,  $Fr = 1.0$ ;  $\square$ ,  $Re = 12700$ ,  $Fr = 8.0$ .

velocity–vorticity correlations in the dynamics of the free-surface jets examined here. We can solve (5) for the velocity–vorticity correlations to get

$$\overline{u\omega_y} - \overline{v\omega_x} = \frac{\partial}{\partial z}(k - \overline{w^2}). \quad (7)$$

This equation shows that the velocity–vorticity correlations are equal to the gradient of  $(k - \overline{w^2})$ . For a deep jet  $k$  is generally larger than  $\overline{w^2}$  and both are positive, so the gradient in  $(k - \overline{w^2})$  will be positive below the jet axis and negative above. For a jet near the free surface, the above-described vortex/free-surface interaction should cause the gradient in  $(k - \overline{w^2})$  to be reversed.

Figure 22 shows vertical profiles of  $(k - \overline{w^2})$  for the three jets at  $x/d = 16$  and 32. Far below the jet axis at both locations, the gradient in  $(k - \overline{w^2})$  is positive, as expected for the deep jet. At  $x/d = 16$ , above the jet axis, the high-Froude-number jet still shows a general decrease in  $(k - \overline{w^2})$  as the free surface is approached, and the gradient in  $(k - \overline{w^2})$  at the free surface is comparable in magnitude to that far below the jet axis. For the two low-Froude-number cases, the gradient in  $(k - \overline{w^2})$  changes as the free surface is approached with the high-Reynolds-number jet showing a negative gradient and the intermediate case exhibiting an approximate zero gradient. At  $x/d = 32$  (figure 22a), the gradient in  $(k - \overline{w^2})$  at the free surface has taken on a definite positive value for all three cases. This shows that the velocity–vorticity correlations in (5) and (6) are now clearly positive.

These results show that the velocity–vorticity correlations are positive, as expected, near the free surface at  $x/d = 32$ , but not at  $x/d = 16$ . At  $x/d = 16$  the vorticity–velocity correlations for the high-Reynolds-number jet are positive but not as large as at  $x/d = 32$ . This may indicate that the correlations evolve in the streamwise direction, and are small in magnitude near the initial interaction (possibly due to the requirement that material must be accelerated in the plane of the surface to yield a positive correlation). This difference may also be due, in part, to the larger surface disturbances at  $x/d = 16$  compared to those at  $x/d = 32$ . At  $x/d = 16$ , the velocity–vorticity correlations for the high-Froude-number case have not been significantly affected by the presence of the free surface while those for the intermediate case (with equal Reynolds number, but lower Froude number) have. This also indicates that the surface disturbances play a role in suppressing the natural interaction of tangential vorticity with a free surface and is consistent with the Froude-number

dependence in the partitioning of the turbulence kinetic energy among the vertical and tangential velocity fluctuations identified above (§3.3).

It has been proposed here that interaction of tangential vorticity with the free surface results in the spreading of the jet at the surface. The smaller velocity–vorticity correlations seen in the high-Froude-number jet are also consistent with the observed smaller lateral spreading velocity at the free surface for this case.

Shadowgraph images showed that, in the case of the high-Reynolds-number jet, there is evidence of multiple reconnection to their ‘images’ of long vortex filaments near the free surface in a manner reminiscent of the vortex-pair instability of Crow (1970). It has been proposed above in §3.1 that for high-Reynolds number flows, the tangential vorticity can exist near the free surface for a considerably longer time than for low-Reynolds-number flows. As a result, the vorticity can interact with its ‘image’ for a longer period. In figure 22, the high-Reynolds-number jet exhibited a larger gradient in  $(k - \overline{w^2})$  near the free surface (larger velocity–vorticity correlations) than for the low-Reynolds-number case at the same Froude number (particularly at  $x/d = 16$ ). The increase in the velocity–vorticity correlations near the free surface is consistent with the observations of more persistent (longer lived) tangential vorticity near the free surface.

Dye visualization also identified a turbulent ‘core’ region below the surface which was confined to roughly  $|y/x| \leq 0.10$ . In the turbulence measurements, the core region was shown to be above roughly  $z/x = -0.1$ . Inside the core, more energy is contained in the streamwise velocity fluctuations than in the other two velocity components. Outside the core, the fraction of energy contained in the radial component of velocity increases. The radial component corresponds to  $w$  on the vertical symmetry plane and  $v$  on the free surface. The increase in the fraction of turbulence kinetic energy contained in these velocity components is associated with the entrainment field on the centreplane and the diverging flow at the free surface. For the high-Froude-number case there is an additional increase in the fraction of kinetic energy in the  $v$ -fluctuations the free surface for  $y/x > 0.15$ . There is also a slight increase in the fraction of  $k$  contained in the  $w$ -fluctuations for this region in the high-Froude-number case, as well as a reduction of the correlation coefficient for  $\overline{uv}$ . The reduction in  $R_{uv}$  indicates that the increase in energy results from either uncorrelated velocity fluctuations, or fluctuations in  $u$  and  $v$  which are  $\frac{1}{2}\pi$  out of phase. The latter is the case for orbital velocities associated with wave motion. In light of the large surface disturbances identified in the high-Froude-number case and the fact that the resulting waves propagate nearly perpendicularly to the jet axis, we (like Anthony & Willmarth 1992) will attribute this behaviour to the waves generated in this case. This is consistent with the observation of lower turbulence kinetic energy in the high-Froude-number case, and supports the proposition that the turbulence energy has been transferred to the wave field.

Figures 14, 15 and 16 revealed that the partitioning of the turbulence kinetic energy among the three components of the fluctuating velocity near the free surface was Froude-number dependent. To refine this idea we can examine how  $\overline{u_i u_i}/2k$  (no sum on  $i$ ) depends on local Froude number. For the two different  $x/d$ -locations and the conditions examined, the estimated local Froude numbers are shown in table 3. For the flows examined, the local Froude numbers range from about 1.8 down to 0.09 and, as expected, the local Froude numbers are roughly the same for flows with equal Froude numbers based on jet-exit conditions. The highest local Froude numbers occur near the jet exit ( $x/d = 16$ ) for the high-Froude-number case, and the low Froude-number cases have lower Froude numbers for both locations than for both locations in the high-Froude-number case.

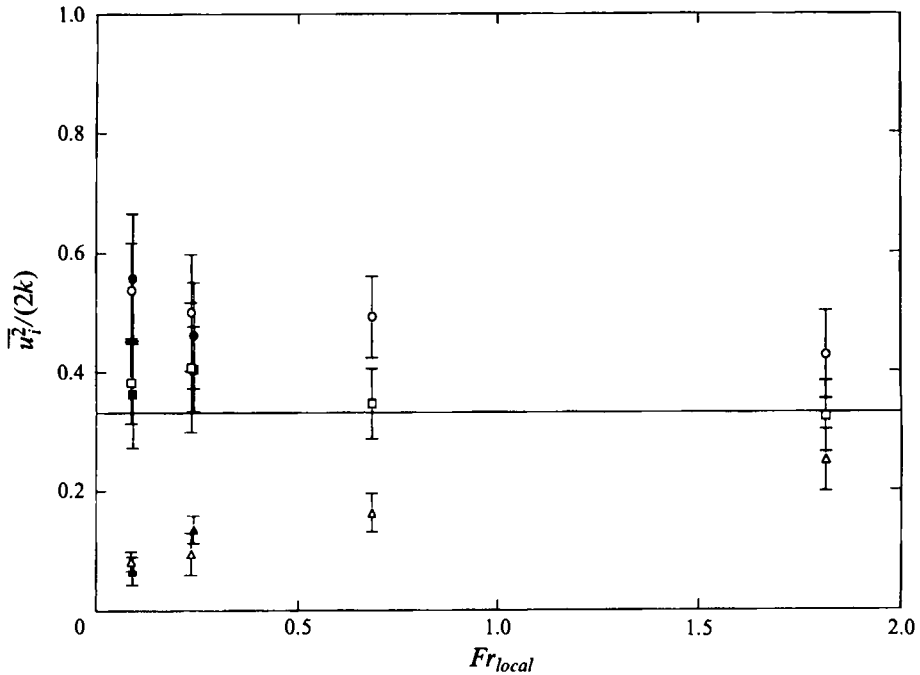


FIGURE 23. Variation of  $\overline{u_i^2}/2k$  at the free surface with local Froude number:  $\circ$ ,  $\overline{u^2}/2k$ ;  $\square$ ,  $\overline{v^2}/2k$ ;  $\triangle$ ,  $\overline{w^2}/2k$ . Open symbols are for  $Re = 12700$ , solid symbols are for  $Re = 102000$ . Symbol plotted at the mean free-surface value; error bars indicate two standard deviations.

Figure 23 shows the fraction of  $k$  in the various fluctuating velocity components near the surface versus local Froude number for the cases examined. The mean value of the data from the horizontal profiles is plotted with error bars indicating an interval of  $\pm 2$  standard deviations. The horizontal line is located at  $\overline{u_i^2}/2k = 1/3$ , the value for homogeneous isotropic turbulence. (In examining this figure, it is important to keep in mind that the local Froude number decreases with increasing streamwise distance. Hence, an increase in Froude number means that you have moved closer to the jet origin.) For high Froude numbers, the anisotropy is less pronounced;  $\overline{u^2}/2k$  is the largest,  $\overline{v^2}/2k$  is near  $1/3$  (slightly larger) and  $\overline{w^2}/2k$  is less than  $1/3$ . As the Froude number decreases,  $\overline{w^2}/2k$  decreases dramatically and the magnitudes of  $\overline{u^2}/2k$  and  $\overline{v^2}/2k$  increase, with roughly two-thirds of the decrease in  $\overline{w^2}/2k$  going to  $\overline{u^2}/2k$  and one-third going to  $\overline{v^2}/2k$ . This means that the energy which is contained in the  $w$ -fluctuations at high Froude number is redistributed primarily to the  $u$ -fluctuations by the presence of the free surface. (These changes represent redistribution of energy since  $\overline{u^2} + \overline{v^2} + \overline{w^2} = 2k$  by definition.) Since the large energy-containing scales of the jet are contained in vortical structures which comprise in large part of transversely ( $y$ -direction) oriented vorticity near the free surface, it is more likely that the  $\overline{w^2}$  energy will be transferred to  $\overline{u^2}$ . This would imply that to the two velocity-vorticity correlations examined above in combination,  $\overline{u\omega_y}$  is larger than  $-\overline{v\omega_x}$ . In other words, the mean flow determines a preferred orientation for the vorticity as it approaches the surface, and this results in a preferred mode for the redistribution.

This transfer of energy near the free surface is in contrast to the behaviour seen in turbulent open channel flow by Handler *et al.* (1993). In that study, the energy contained in the surface-normal velocity fluctuations was transferred to the transverse,

rather than streamwise, fluctuations. This difference may be due to the nature of the dominant vortical structures for the two flows. In the channel flow hairpin-type structures are generated near the wall and then rise to the free surface. The elongation of the legs of the vortices results in significant streamwise-oriented vorticity. The transfer of energy to the transverse velocity may result from interaction of this streamwise vorticity with the free surface. Hence, the same type of vorticity/free-surface interaction can account for the observed behaviour in both the channel flow and the jet, although they lead to different results in the redistribution of energy.

Since the motivation for this study was to obtain information useful in predicting the flow around a ship and in the wake, a few words about the implications of these results for that problem are in order.

Near the ship, the Froude number for the turbulent wake is high, comparable to the high-Froude-number case examined here. This means that significant wave generation will occur with a corresponding loss of turbulence kinetic energy from the subsurface flow to the wavefield. The level of kinetic energy at any given location in the flow field will have a first-order effect on the evolution of the flow downstream, and so representing this energy transfer accurately is critical to accurate predictions. The energy transfer results from inherently unsteady behaviour, and therefore is not captured in Reynolds-averaged turbulence models implicitly and hence must be modelled in some fashion. The details and mechanisms associated with this transfer are, at present, not well-enough understood to attempt this modelling on a rational basis. It is possible that large-eddy simulations would be able to capture a significant portion of the transfer, but calculations with a full deformable free surface, capable of handling steep disturbances, will be required.

Both near the ship and far aft in the wake, the Reynolds number for the flow will remain high, and the behaviour of the flow will be characterized by the interaction of the turbulent vorticity field with the free surface. The diverging flow at the surface caused by the interaction of tangential vorticity with the free surface, which is more pronounced at low Froude number, will be an important feature in this region. (There is evidence that this behaviour is modified by the presence of surfactants, but that only makes things more complicated; see, e.g. Anthony & Willmarth 1992 and Reed *et al.* 1990.) The vortex/free-surface interaction which contributes to the diverging flow also redistributes energy from the surface-normal to tangential velocity fluctuations. This interaction must be modelled appropriately to produce accurate results. Large-eddy simulations should, in principle, be able to predict directly the portion of the diverging flow at the free surface which originates in the large scales; however, the portion of the diverging flow which results from the interaction of the small scales with the free surface will require additional modelling at subgrid scale.

#### 4. Conclusions

In this study, the effects of the main parameters, Froude number and Reynolds number, on the structure of turbulence in near-surface turbulent jets, and the interaction between the subsurface turbulence and the free surface were examined. Measurements of all six Reynolds stresses and the three mean velocity components were obtained, as well as qualitative visualization. Three jet flows were investigated; the baseline case was at  $Re = 12700$  and  $Fr = 1.0$ . Reynolds-number effects were investigated by examining a jet at  $Re = 102000$  and  $Fr = 1.0$ , while Froude-number effects were investigated by examining a jet at  $Re = 12700$  and  $Fr = 8.0$ . This combined set of results allows a comprehensive evaluation of the effects of these

parameters over a meaningful range. The measurements were confined to vertical profiles on the jet axis and horizontal profiles at the free surface for two streamwise locations,  $x/d = 16$  and  $32$ . The major conclusions of the study are summarized below.

Interaction of turbulent shear flows with a free surface:

(i) For a nearly flat free surface, vorticity which is tangential to the surface interacts with its 'image' above the surface. This causes the velocity–vorticity correlations  $(\overline{u\omega_y} - \overline{v\omega_x})$  to be positive and yields a decrease in  $\overline{w^2}$  as the free surface is approached. The energy which is removed from the surface-normal velocity fluctuations by this mechanism is transferred to the tangential fluctuations.

(ii) The interaction embodied in the velocity–vorticity correlations requires some streamwise distance to develop, and so the transfer of energy from the surface-normal to tangential velocity fluctuations increases with downstream distance.

Froude-number effects:

(i) At high Froude number, energy is transferred from the subsurface turbulence to the surface waves as a result of large-amplitude free-surface disturbances generated by the turbulence. This results in turbulence kinetic energy levels which are lower by as much as 20% in the high-Froude-number jet, compared to the low-Froude-number jets. For this case, there were also higher r.m.s. velocity fluctuations and lower correlation coefficients outside the core region in the high-Froude-number jet which is consistent with larger wave amplitudes.

(ii) At high Froude number, where surface disturbances are large, the interaction of the tangential vorticity with its image is diminished and little energy is transferred from the surface-normal to tangential velocity fluctuations near the free surface.

(iii) As the local Froude number decreases, roughly two-thirds of the energy removed from the surface-normal velocity fluctuations is transferred to the streamwise fluctuations and one-third to the transverse fluctuations. This may be due to the preferred transverse orientation of the vorticity near the surface in the initially axisymmetric jets examined here.

(iv) At high Froude number, the Reynolds shear stresses  $\overline{uw}/U_0^2$  and  $\overline{vw}/U_0^2$  are smaller than those for the low-Froude-number jets. The difference results directly from the low  $u'$ ,  $v'$  and  $w'$  levels (resulting from loss of turbulence kinetic energy to wave generation) and not from decreased correlation in the turbulent velocity fluctuations.

Reynolds-number effects:

(i) For the high-Reynolds-number jet the local Reynolds number increases more slowly, and the local Froude number decreases more slowly, with streamwise distance than for the low-Reynolds-number jets. Hence, the high-Reynolds-number jet evolves more slowly in the presence of the free surface than the low-Reynolds-number jets.

(ii) At high Reynolds number tangential vorticity can persist longer near the free surface than for low Reynolds number. This results in a measurable increase in the velocity–vorticity correlations at the free surface; however, the effect is not significant enough to alter the outward flow at the surface over the range of streamwise locations examined.

This work was supported by the Fluid Dynamics Program of the Office of Naval Research under Grant Number N00014-92-J-1750 and as part of the University Research Initiative/Program in Ship Hydrodynamics under Contract Number N00014-86-K-0684. The help of Dr D. G. Anthony late of the David Taylor Model Basin in setting up the laser velocimeter and flow visualization, and in providing access to his data in the early stages of this investigation, is greatly appreciated.

## REFERENCES

- ANTHONY, D.G. 1990 The influence of a free surface on the development of turbulence in a submerged jet. PhD thesis, University of Michigan.
- ANTHONY, D. G. & WILLMARTH, W. W. 1992 Turbulence measurements in a round jet near a free surface. *J. Fluid Mech.* **243**, 699–720.
- BROWN, J. L. 1989 Geometric bias and time coincidence in 3-dimensional laser Doppler velocimeter systems. *Exps Fluids* **7**, 25–32.
- CROW, S. C. 1970 Stability theory for a pair of trailing vortices. *AIAA J.* **8**, 2172–2179.
- DAVIS, M. R. & WINARTO, H. 1980 Jet diffusion from a circular nozzle above a solid wall. *J. Fluid Mech.* **101**, 201–221.
- DUNCAN, J. H. 1983 The breaking and non-breaking wave resistance of a two-dimensional hydrofoil. *J. Fluid Mech.* **126**, 507–520.
- HANDLER, R. A., SWEAN, T. F., LEIGHTON, R. I. & SWEARINGEN, J. D. 1993 Length scales and the energy balance for turbulence near a free surface. *AIAA J.* **31**, 1998–2007.
- HECHT, E. & ZAJAC, A. 1974 *Optics*. Addison-Wesley.
- HINZE, J. O. 1975 *Turbulence*, 2nd edn. McGraw-Hill.
- HIRSA, A. & WILLMARTH, W. W. 1994 Measurements of vortex pair interaction with a clean or contaminated surface. *J. Fluid Mech.* **259**, 25–45.
- HOEKSTRA, M. 1991 Macro wake features of a range of ships. *MARIN Rep.* 410461-1-P. Maritime Research Institute Netherlands.
- HUNT, J. & GRAHAM, J. 1978 Free stream turbulence near plane boundaries. *J. Fluid Mech.* **84**, 178–209.
- LAUNDER, B. E. & RODI, W. 1983 The turbulent wall jet – measurements and modeling. *Ann. Rev. Fluid Mech.* **15**, 429–459.
- LIEPMANN, D. 1990 The near-field dynamics and entrainment field of submerged and near-surface jets. PhD thesis, University of California, San Diego.
- LONGUET-HIGGINS, M. S. & STEWART, R. W. 1961 The changes in amplitude of short gravity waves on steady non-uniform currents. *J. Fluid Mech.* **10**, 529–549.
- MADNIA, K. & BERNAL, L. P. 1984 Interaction of a turbulent round jet with the free surface. *J. Fluid Mech.* **261**, 305–332.
- McLAUGHLIN, D. K. & TIEDERMAN, W. G. 1973 Biasing correction for individual realization laser anemometer measurements in turbulent flow. *Phys. Fluids* **16**, 2082–2088.
- REED, A. M., BECK, R. F., GRIFFIN, O. M. & PELTZER, R. D. 1990 Hydrodynamics of remotely sensed surface-ship wakes. *Trans. Soc. Naval Archit. Mech. Engrs* **98**, 319–363.
- STERLING, M. H., GORMAN, M., WIDMANN, P. J., COFFMAN, S. C., STROZIER, J. & KIEHN, R. M. 1987 Why are these disks dark? The optics of Rankine vortices. *Phys. Fluids* **30**, 3624–3626.
- SWEAN, T. F., RAMBERG, S. E., PLESNIA, M. W. & STEWART, M. B. 1989 Turbulent surface jet in a channel of limited depth. *J. Hydraulic Engng* **115**, 1587–1606.
- TENNEKES, H. & LUMLEY, J. L. 1972 *A First Course in Turbulence*. MIT Press.
- WALKER, D. T. & JOHNSTON, V. G. 1991 Observations of turbulence near the free surface in the wake of a model ship. In *Dynamics of Bubbles and Vortices Near a Free Surface* (ed. I. Sahin & G. Tryggvason). AMD-119. ASME.
- WHIFFEN, M. C., LAU, J. C. & SMITH, D. M. 1979 Design of LV experiments for turbulence measurements. In *Laser Velocimetry and Particle Sizing* (ed. H. D. Thompson & W. H. Stevenson), pp. 197–207. Hemisphere.
- WILLMARTH, W. W. 1987 Design of a three-component fiber-optic laser-Doppler anemometer for wake measurements in a towing tank. *Proc. Intl Towing Tank Conf. ITTC*, Tokyo.
- WYGANANSKI, I. & FIEDLER, H. 1969 Some measurements in the self-preserving jet. *J. Fluid Mech.* **38**, 577–612.